A Geophysical Study of the Hill's Pond Lamproite

Woodson and Wilson Counties, Kansas

by

Mary Anne Markezich

B.S. University of New Orleans, 1985

Submitted to the Department of Geology and the Faculty of the Graduate School of the University of Kansas in partial fulfillment of the requirements for the degree of Master of Science.

Professor in Charge

Committee Members

For the Department

July 22, 1988

Date thesis accepted

Kansas Geological Survey
Open-file Report

Disclaimer

The Kansas Geological Survey does not guarantee this document to be free from errors or inaccuracies and disclaims any responsibility or liability for interpretations based on data used in the production of this document or decisions based thereon. This report is intended to make results of research available at the earliest possible date, but is not intended to constitute final or formal publication.

ABSTRACT

Silver City Dome is located in southeastern Kansas in Woodson and Wilson counties. It was formed about 90 million years ago by the intrusion of the Hill's Pond lamproite into Pennsylvanian sedimentary rocks. The dome, which covers an area of 21.5 square kilometers, is an elliptical, anticlinal structure which is eroded in the center and is surrounded by steeply-dipping edges. The interior portion shows a gently-rolling topography made up of anticlines and synclines whose axes trend in an east-west direction. Wagner (1954) interpreted that magma rose along a north-dipping fault located in the northern part of the dome and then penetrated southward into the sedimentary sequence forming numerous sills. The intrusion is significant because it is one of only a few igneous intrusions exposed at the surface in Kansas.

Geophysical studies at the dome from 1985 to 1987 provide an expanded interpretation of its formation. These studies included two seismic reflection surveys and a magnetic survey. In 1985, seismic data were collected to provide insight on the dome's structure and to detect the locations of the sills. The seismic line transected the dome in a north-south direction and extended beyond the edges; thus, a general idea of the structure of the dome

was obtained. These data showed that the dome is bounded at both edges by marginal grabens. The data also show two different scales of doming: a broad, gentle dome over the entire structure and a smaller dome located near the northern edge. In 1986 and 1987, additional data collected with a higher-frequency source revealed a seismically-chaotic zone located at a depth of approximately 750 meters near the north part of the dome. The material within this zone is interpreted to consist of shattered country rock mixed with igneous rock which came up from deep within the earth and is proposed to be the source of the sills. This source is closer to the center of the dome than the source proposed by Wagner. A zone of sills interlayered with metamorphosed sedimentary rocks overlies the source region and has been detected seismically as high-amplitude, low-frequency events. A fracture zone, which bounds the intruded region on the north and connects to the principal magma body with depth, could have served as a conduit for the magma. Magnetic data were collected in the northern part of the dome and were used in a qualitative sense as support for the seismic data.

TABLE OF CONTENTS

TABLE OF CONTENTS (CONTINUED)

LIST OF ILLUSTRATIONS

LIST OF ILLUSTRATIONS (continued)

LIST OF TABLES

PAGE

ACKNOWLEDGEMENTS

I would like to thank Ralph Knapp for all the help he has given me. He was always willing to answer any questions I asked, and his confidence in my ability has meant a lot to me. My other committee members, Don Sprowl and Pat Bickford, gave useful editing suggestions for my thesis. In addition, Dr. Bickford provided information on much of the geologic background for this thesis. Geologic insight given by Krzysztof Wojcik was invaluable. Rick Miller helped answer some of my data processing questions. Pieter Berendsen provided articles as well as slides of Silver City Dome.

The Graphic Arts Department at Nicholls Hall did excellent work on the figures they prepared for my SEG talk. I was able to use some of these figures in my thesis, and that saved me many headaches when it came time for figure preparation. The color plots in this thesis were created on a Landmark Graphics Corporation Desktop Workstation. I am indebted to Landmark for letting the KGS use this system.

I would like to thank the following people who helped collect the data for my thesis: Jeff Treadway and Paul Myers (operators of the seismic recording truck), Ralph Knapp, Krzysztof Wojcik, Rick Miller, Mary Daily, Dao Somanas, Young Chung, Matt Wilson, Ertan Muftuoglu,

Chong Dae Chung, Jennifer Fesperman, Tonja Nuss, Dana Adkins-Heljeson, and Changlan Yin. Andrew Kalik helped me by taking time to listen to some of my ideas.

I would like to thank my friends from McCollum Hall, especially John Moschella, who helped me to keep my sanity when things got rough. I am grateful to my parents and brother for the emotional support they have given me not only at KU, but all my life. Last, but certainly not least, I would like to thank Bryan Stephens for his encouragement and friendship.

INTRODUCTION

SILVER CITY AND ROSE DOMES

Silver City Dome is located in southeastern Kansas (Sec. 32, T. 26 S., R. 15 E.) (Figure 1) in the northern part of the Cherokee Basin and is believed to have formed by the intrusion of the Hill's Pond Lamproite into the Pennsylvanian sedimentary rocks. The dome is elliptical in shape and covers an area of 21.5 square kilometers (Figure 2).

The geologic map (Figure 3) shows that the dome has been eroded in the center and is bounded by steeply-dipping beds. The interior of the dome shows a gently-rolling topography. Regionally, the sedimentary rocks in this area strike N20E and dip to the northwest at about 4.8 meters per kilometer (Wagner, 1954). A series of northwest-trending folds are superimposed on this regional dip. The Fredonia anticline, which occurs south of Silver City Dome, is one such fold whose axis trends N45W. The axes of another series of folds trend in a S45W direction from the dome. The Upper Pennsylvanian Stanton Formation, Weston Shale, and Stranger Formation crop out in the center of the dome. Lamproite is also exposed as shown by the stippled pattern. The fault at the north edge of the lamproite is described only as "apparently dipping north at a high angle" (Wagner, 1954). Magma is thought to have risen

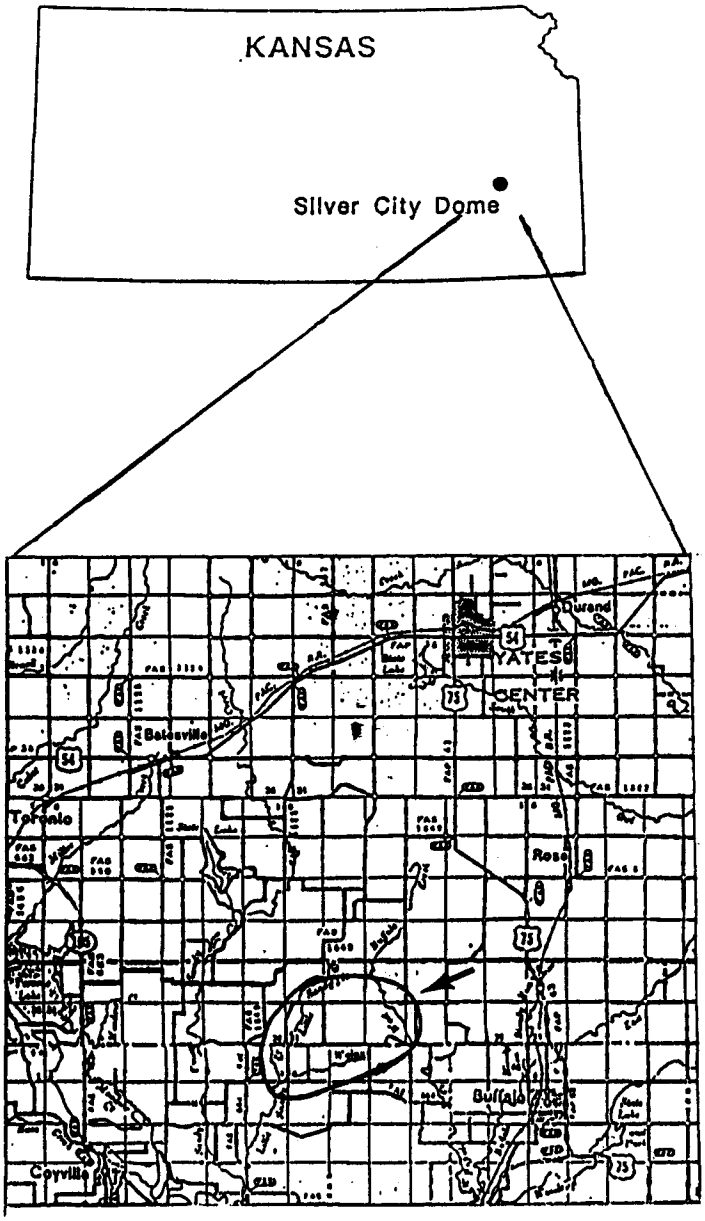

Figure 1. Location of Silver City Dome in southeastern Kansas.

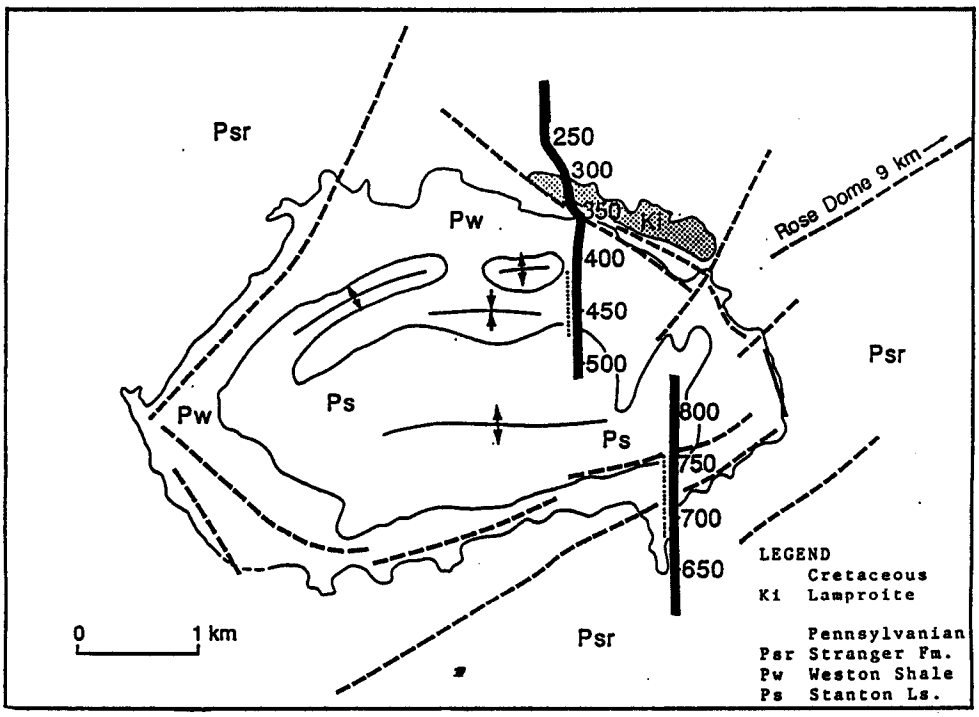

Figure 2. The elliptical shape of Silver City Dome is outlined by lineaments shown by dashed lines. Heavy lines are the position of the seismic line collected in 1985, and the numbers along these lines are the locations of the common midpoints (CMPs). Dotted lines between CMPs 300 and 330 and between CMPs 675 and 760 indicate the northern and southern grabens, respectively. The collapsed zone is shown by the dotted lines between CMPs 400 and 480 (from Wojcik, 1986).

GEOLOGY OF NORTHERN SILVER CITY DOME

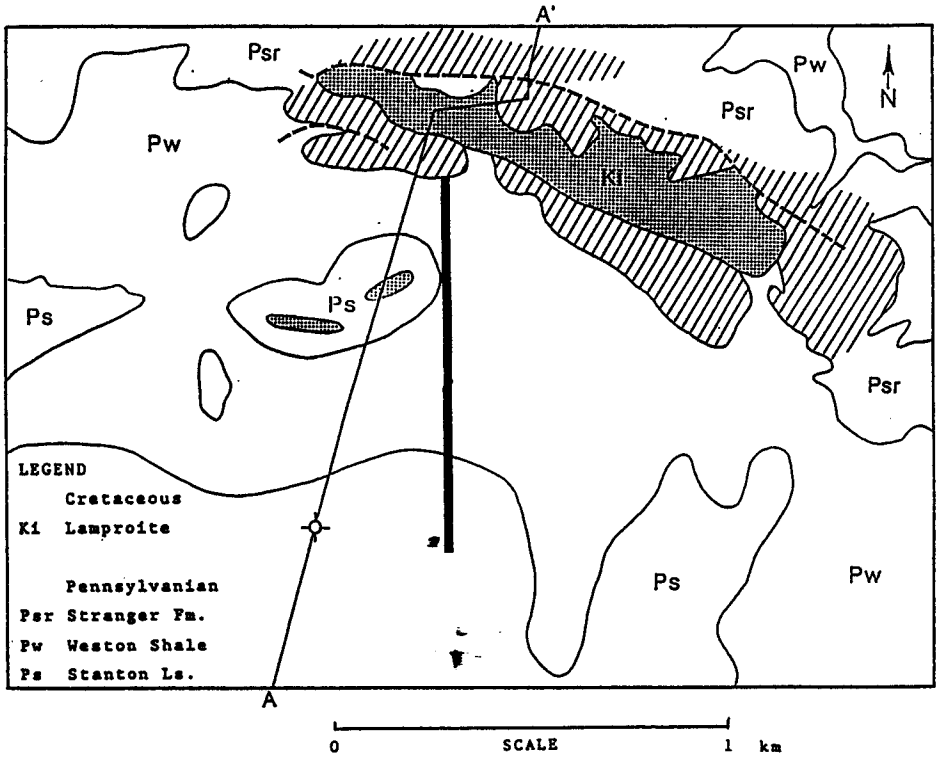

Figure 3. Generalized version of the geology of the northeastern corner of Silver City Dome (from Wagner, 1954). Stippled pattern shows the outcrop of the lamproite. Lined pattern shows the metamorphic aureole surrounding the intrusion. The heavy, dashed line is the steeply-dipping fault described by Wagner to be the pathway for the magma. Franks (1959) reports a nine-meter-thick sill at an approximate depth of 230 meters at the well located along the line of the cross-section. Heavy line is the location of the seismic data collected in 1986 and 1987.

along the fault, with lamproite sills injected to the south into the Pennsylvanian sequence as illustrated in the cross-section shown in Figure 4. The alternating layers of shale and limestone within these Pennsylvanian cyclothems make good pathways along which magma can easily move. Wagner (1954) stated that the thickness between the top of the Mississippian and the base of the Kansas City Group was increased by more than 60 meters in places. A 9-meter-thick sill at approximately 230 meters depth has been reported from a drill hole which is located along the line of the cross-section (Franks, 1959).

A 300-meter-wide contact metamorphic aureole is noted around the outcrop of the lamproite on the north flank of the dome as shown by the lined pattern on the map. During the metamorphism, sandstones were converted to quartzites, and chlorite was developed. In addition, epidote, tremolite-actinolite, hornblende, and chert were formed in limestone and calcareous shale (Wagner, 1954).

Lamproites, a type of peridotite, are mafic to ultramafic alkaline igneous rocks which have higher K/Na and K/Al ratios than other igneous rock types. They do not contain plagioclase, and many possess a glassy groundmass. Petrographically, they are very diverse, but they are defined by their major and accessory mineral content, alteration products, and mineral paragenesis (Bergman,

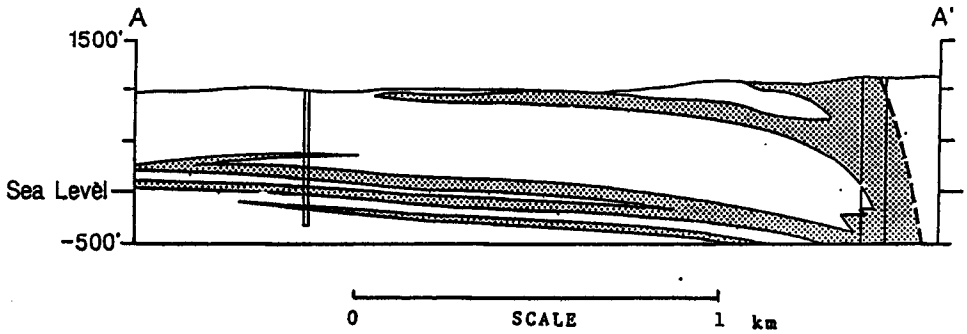

Figure 4. Generalized cross-section showing Wagner's interpretation of the formation of Silver City Dome. The heavy, dashed line is the steeply-dipping fault interpreted to be the conduit for the rising magma. The stippled pattern shows the lamproite sills. The drill hole near the southern end of the section records sills at a depth of approximately 230 meters (765 feet). The two, solid, vertical lines at the north end are bends in the line of section (from Wagner, 1954).

1987). A list of some of these characteristic features of lamproites is given in Appendix A. The following minerals are commonly found in lamproites: leucite, K-richterite, phlogopite, diopside, olivine, sanidine, priderite, perovskite, wadeite, apatite, chrome spinel, and ilmenite. Lamproites have been noted in 22 localities on 6 continents. In Figure 5, the circles are lamproite localities whereas the squares are locations of other potassic and ultrapotassic rocks. Prior to the late 1970's, kimberlites were the only igneous rocks to be associated with diamonds. Since this time, some lamproites have been found to contain diamonds. The Prairie Creek kimberlite in Murfreesboro, Arkansas (Pike County) has been reclassified as a lamproite, whereas other diamond-bearing lamproites have been found at two locations in western Australia, one of which had diamonds present in over 30 intrusions. These discoveries have increased the importance of lamproites in terms of economics and petrogenesis (Bergman, 1987).

The Hill's Pond lamproite is believed to have been emplaced non-violently as a primarily liquid intrusion. Evidence for this type of intrusion is the evident injection of magma as thin sills and the presence of ophitically-intergrown phlogopite (Merrill et al., 1977). Cullers et al. (1985) concluded that the lamproite magma

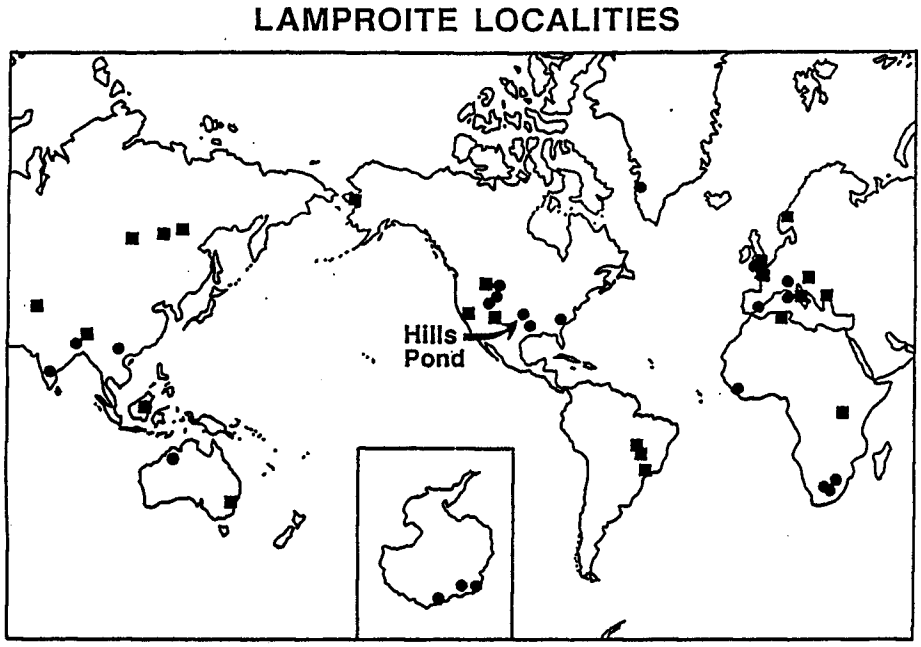

Figure 5. Lamproites have been found in 22 localities across the world. Circles represent lamproite localities while the squares represent locations of other potassic and ultra-potassic rocks (from Bergman, 1987).

was probably formed by melting of upper mantle garnet peridotite. Crystallization of the magma formed a porphyritic mica lamproite with a groundmass consisting of phlogopite and serpentine. Phenocrysts include serpentinized olivine, augite, richterite, and phlogopite. Accessory minerals include apatite, perovskite, and chrome spinel. At the surface, the lamproite has been weathered to a soil which is composed predominantly of clay minerals. The lamproite was determined by K-Ar dating methods to be 90 million years old which is Late Cretaceous. Diamonds have not been found in the Hill's Pond lamproite even though its geochemistry is almost identical to at least three diamond-bearing lamproite suites. If the source conditions for the generation of the Hill's Pond magma were similar to those which formed the diamond-bearing magmas, then the absence of diamonds in the Hill's Pond lamproite may be explained by the quiet nature of the intrusion which did not allow the preservation of diamonds (Bergman, 1987).

Rose Dome (Figure 6; Merriam, 1963) lies five miles northeast of Silver City Dome and was also formed about 88 million years ago by the intrusion of lamproite magma into Pennsylvanian sedimentary rocks. The lamproite at Rose Dome is not exposed at the surface. It is composed of phlogopite, serpentinized olivine remnants, diopsidic augite, and amphibole in a serpentinized groundmass.

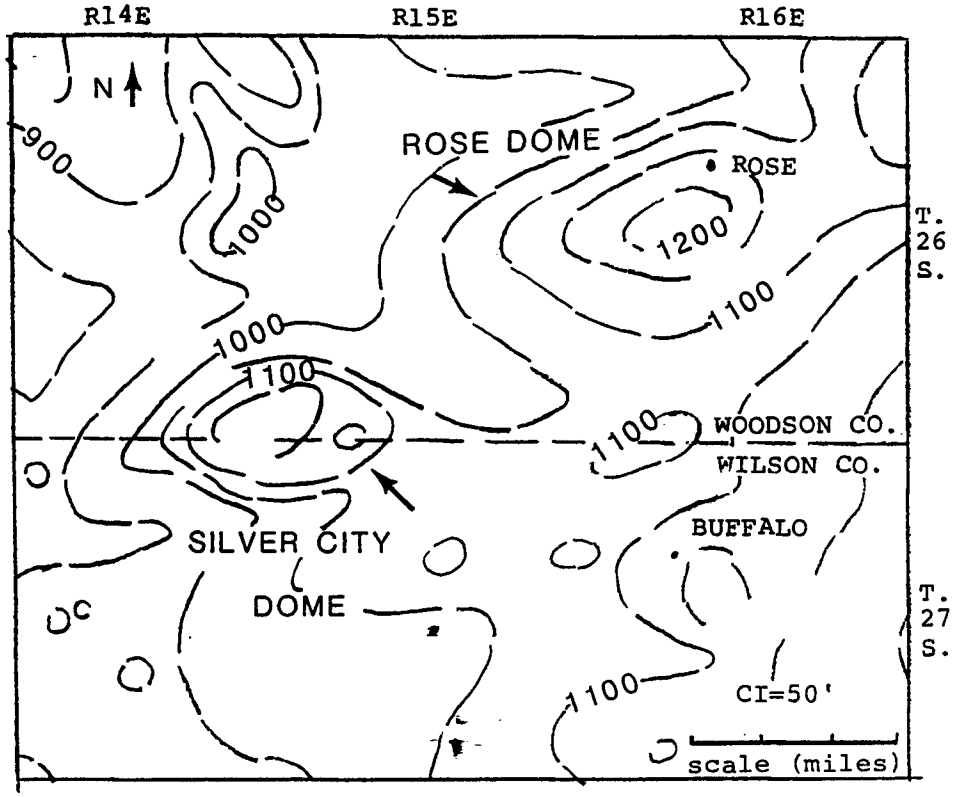

Figure 6. Structure map of the base of the Missourian Plattsburg limestone showing the relationship between Rose and Silver City Domes (from Hambleton and Merriam, 1955).

Apatite, magnetite, and iron chromite occur as accessory minerals. The presence of granite boulders found on the surface at Rose Dome was once a confusing issue. These boulders were found in 1916 over an area of approximately 120 acres. Various ideas such as stream and glacial transport were raised as to how these granites came to be found at Rose Dome (Twenhofel, 1917, 1919, 1926). They are now interpreted to have been transported from the Precambrian basement as xenoliths within the uprising magma. These xenoliths are composed of microcline perthite, plagioclase, quartz, and biotite. Zircons separated from the granite yield U-Pb ages of 1408 ± 21 Ma (Bickford et al., 1981). Because the xenoliths have a lower density than the lamproite, they are believed to have been concentrated in the upper part of the magma (Franks et al., 1971). Textures of the granite range from very coarse-grained and inequigranular to fine-grained and equigranular. Parts of the rock show flow structures and alignment of granitic rock fragments in a fine-grained matrix composed of quartz and feldspar. The flow texture appears to have formed later than the other textures because it encompasses all of them. This flow texture, plus the presence of co-existing high-temperature and low-temperature feldspars, indicate that the granite underwent partial melting as it was carried in the magma. Magmatic

emplacement caused extensive contact metamorphism of the surrounding Pennsylvanian sedimentary rocks. The Weston shale was metamorphosed into a sanidine-magnesian biotite hornfels, while the Stanton Limestone was recrystallized into a brucite-bearing marble. The presence of sanidinite facies metamorphism indicates high-temperature (700-840°C) and low-pressure conditions (200-300 bars) at the time of emplacement. Other evidence for high-temperature and low-pressure conditions includes the partial melting of the granite, presence of stumpy quartz crystals which resemble high quartz, and presence of andalusite in vuggy quartz in both the granite and the lamproite. The system is believed to have been wet during the intrusion of the magma. Evidence includes vuggy quartz, large amounts of phlogopite, and extensive contact metamorphism (Franks et al., 1971, Bickford et al., 1971, Zartman et al., 1967).

The intrusion at Rose Dome appears to be genetically related to that at Silver City Dome. Figure 2 shows that Rose and Silver City Domes appear to be aligned along a series of faults which trend in a northeast-southwest direction. In addition, textural and structural evidence in both areas indicate that the lamproite magma was emplaced gently as a liquid intrusion with crystals of olivine, phlogopite, pyroxene, and amphibole already formed.

Snyder and Gerdemann (1965) believed that Rose and Silver City Domes are the westward extension of a 400-mile-long-east-west lineament called the 38th parallel lineament by Heyl. The lineament is defined by eight alkalic bodies which penetrate the stable platform as stocks, plugs, sills, and dikes which range in composition from nepheline syenite to alkalic peridotite and range in age from Late Ordovician to Late Cretaceous. These structural features extend across Missouri into Illinois and are shown on the map in Figure 7. Snyder and Gerdemann believe that these structures are genetically related and could be the result of intermittent deep-seated faulting and intrusion over time. Paul (1970) has since interpreted the Decaturville "Disturbance" to be an impact structure. Some of the criteria he used to make this interpretation include the similarity of this structure to known impact structures, the presence of shatter cones, the brecciation of rocks at the center of the structure, and the inward and upward movement of the rock formations at the center. He also stated that the Crooked Creek "Disturbance" and the Weaubleau Structure are probably impact structures as well.

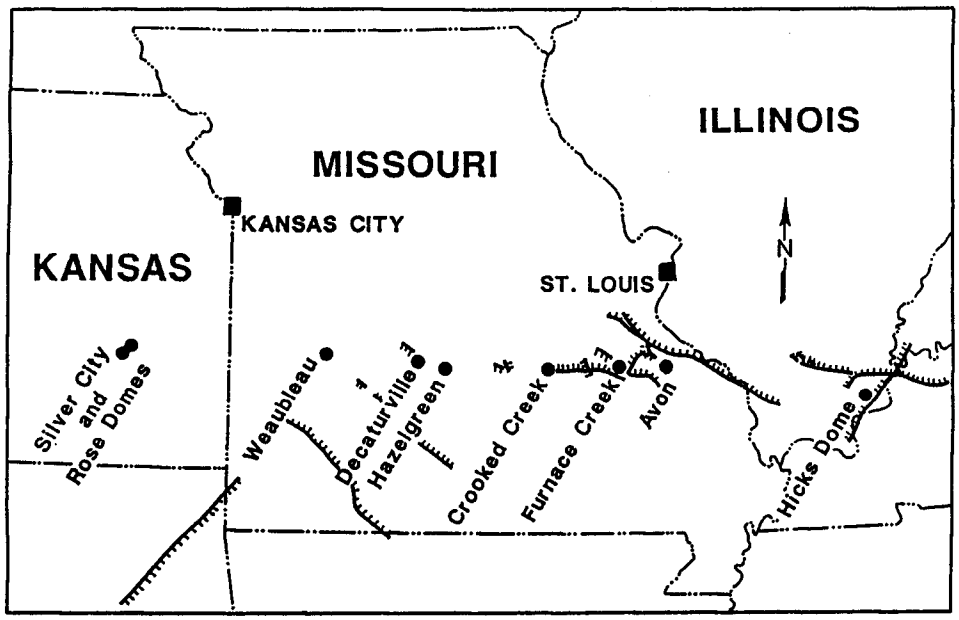

Figure 7. Circles show the nine structural features which form the 38th-parallel lineament of Heyl (from Snyder and Gerdemann, 1965).

PREVIOUS SEISMIC WORK

In 1985, seismic reflection data were collected at Silver City Dome in the areas shown by the heavy lines on the map in Figure 2. The numbers are the Common Midpoints (CMP's) which is a term synonomous with Common Depth Points (CDP's). The purpose of that study was to use reflection seismology to determine the structure of the dome and to attempt to detect the sills. MiniSOSIE earth compactors were used as the source. The final section and an interpretive line drawing are shown in Figure 8.

Krzysztof M. Wojcik, a graduate student at the University of Kansas, processed these data and noticed what appeared to be two scales of doming on the seismic section. The first is a broad, gentle doming over the whole structure. A smaller-scale dome ('a' on Figure 8) is superimposed on the broad dome and occurs to the north of a fractured or collapsed zone (CMP's 400 to 480). Associated with the smaller dome is a depression ('b' in Figure 8). The northern and southern edges of Silver City Dome are bounded by grabens (Figure 8). In Figure 2, some of these features are shown by dotted lines. The northern graben is located between CMP's 300 and 330, whereas the southern graben is located between CMP's 675 and 760. The collapsed zone is located between CMP's 400 and 480. Lineaments,

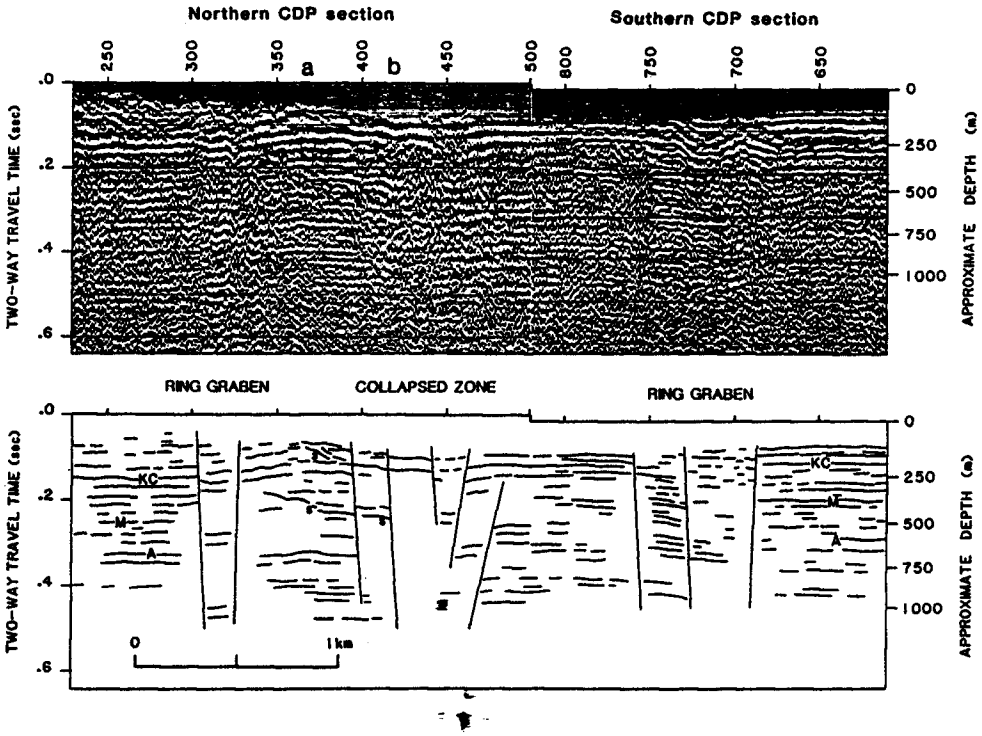

Figure 8. Final seismic section and interpretive line drawing for MiniSOSIE data collected in 1985. Letter 'a' shows the small-scale dome, while letter 'b' shows an adjacent depression. Top of the Arbuckle Group is indicated by 'A'; top of the Mississippian is indicated by 'M'; base of the Kansas City Group is indicated by 'KC'; potential location of lamproite sills is indicated by 'S'.

shown by the dashed lines, outline the elliptical shape of the dome (Wojcik et al., 1987; Wojcik, 1986).

Wojcik's study introduced new ideas on the dome's formation. In addition, it helped to improve the understanding of the structure. It was also concluded that higher resolution data were needed to find the location of the sills.

REGIONAL STRATIGRAPHY

Precambrian rocks in southeastern Kansas include rhyolitic volcanics and epizonal granitic plutons formed about 1380 million years ago (Bickford et al., 1981). The Upper Cambrian and Lower Ordovician Systems are present only in the subsurface in southeastern Kansas. These rocks are mainly dolomites with some limestone, sandstone, and shale and include the Arbuckle Group which consists of crystalline dolomite and contains chert in its upper part. Silurian and Devonian rocks are not represented in southeastern Kansas. The Mississippian System in southeastern Kansas consists of mainly shallow-water carbonates and is present in the subsurface except for an outcrop in the extreme southeast corner of the state. Older Mississippian rocks are only marine, while younger Mississippian rocks are nonmarine as well as marine (Zeller, 1968). Rocks of Middle and Upper Pennsylvanian age consist of laterally-continuous, alternating sandy

shales and limestones which are separated into units called cyclothems. Cyclothems are made up, in ascending order, of a nonmarine, nearshore shale, a transgressive, middle limestone, an offshore shale, a regressive, upper limestone, and another nonmarine, nearshore shale, which is the base of the overlying cyclothem. A generalized stratigraphic section of Pennsylvanian rocks in eastern Kansas is shown in Figure 9.

SEISMIC DATA

ACQUISITION

In 1986, additional seismic data were collected at the Silver City Dome. The data were taken along a section of the 1985 northern line (CMP's 365-485); the purpose of the study was to resolve the events within the collapsed zone and to detect the sills. This time, dynamite was used as the source. Dynamite imparts higher energy and gives higher frequency signals than MiniSOSIE earth compactors. As a result, better resolution was expected because higher frequencies can theoretically detect smaller features. Dynamite was placed in holes which were 3-4 feet deep and spaced 55 feet apart. The maximum and minimum offsets (source-receiver spacing) were set up so that the recorded signal was separated as much as possible from the air-coupled wave, ground roll, and first-break refractions. Maximum offset should be 0.7 to 2 times the depth to the

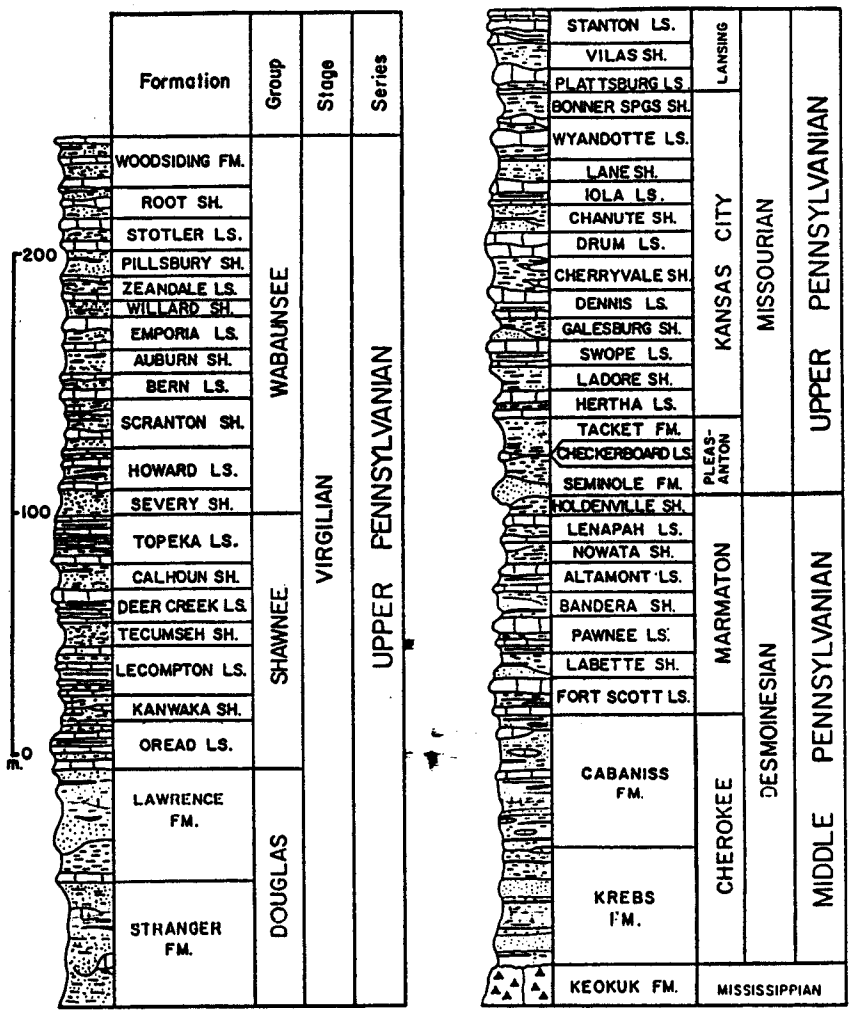

Figure 9. Generalized stratigraphic section of Pennsylvanian rocks in eastern Kansas (from Heckel, 1978, Figure 2).

target reflector (for abrupt velocity changes) while minimum offset should be as close to zero as possible so that first-arrival information is recorded without interference from source-generated noise, ground roll, and the air-coupled wave (Knapp and Steeples, 1986). In order to get a more complete picture of the zone that was proposed to be a potential feeder zone for the lamproite magma, data had to be recorded at least to the basement which was located at a depth of approximately 2500 feet. The geometry of the line was end-on (source to one side of the geophones) with a linear array of geophone groups spaced 55 feet apart which was the maximum spacing for the available cables. End-on geometry was used because all 24 channels of the seismograph were needed so that the receivers could be extended to the maximum offset. An array of 10 equally-spaced (5.5 feet), 30-Hz geophones was used to attenuate the ground roll. The source and receivers were equally spaced so that 12-fold CMP coverage could be obtained. The data were recorded by the Kansas Geological Survey on an I/O DHR 2400 24-channel recording system. The data acquisition parameters are listed in Appendix B. The fold of the data was reduced by half in the center of the line because the spread geometry was changed during the data collection. Half of the data were collected with the source "pulling" the receivers to the

south as shown in Figure 10a, whereas the other half were collected with the source "pushing" the receivers to the south as shown in Figure 10b. The reason for the change in geometry was to extend the data coverage at the southern end of the line. However, the decrease in fold made velocity analysis difficult in this section of the data because coherent reflection events were not easily found as the rocks appeared to be very fractured. In 1987, additional data were collected between CMP's 401 to 480 in an attempt to better analyze the data in the area of the decreased fold. The acquisition parameters were the same as those used in 1986.

PROCESSING

The seismic data were processed on the Kansas Geological Survey's Data General MV20 000 computer using the SPEX package by Sytech Corporation, Houston. Supplementary programs written by R.W. Knapp, Y. Chung, and the writer were also used. The three different acquisition geometries were processed separately with the same processing sequence. The first step in the processing was to convert the raw field data into SEG Y format (Barry et al., 1975) to be compatible with the SPEX programs. Trace editing removed bad traces. Refraction statics and slant stack velocity filter procedures were applied. The data sets were then sorted into CMP gathers and velocity

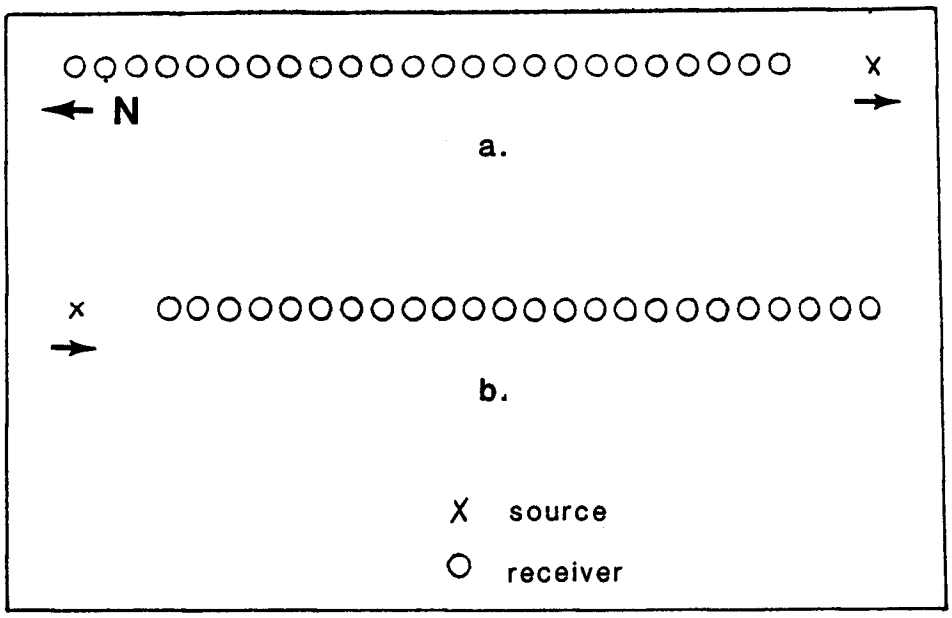

Figure 10. The spread geometry was changed in the middle of the data collection in 1986. a). For the first half of the data collection, the source and receivers were moved to the south with the source in the lead (source "pulling" receivers). b). For the second half of the data collection, the source and receivers were moved to the south with the receivers in the lead (source "pushing" receivers).

analysis was applied. The three data sets were then combined with the necessary static shifts and sorted together to make the final data set. The rest of the processing sequence included deconvolution, velocity analysis, automatic statics, frequency filtering, residual statics, and stacking. Processing parameters for the above sequence are given in Appendix C. Additional processing steps were complex trace analysis and migration. Refraction statics, slant stack, complex trace analysis, and migration are discussed in more detail in Appendices D-G.

INTERPRETATION

The final seismic section and an interpretive line drawing are shown in Figures 11 and 12 respectively. Three distinct areas stand out on the section. These features are as follows: a zone of short, discontinuous reflectors (A), a chaotic zone (B), and a zone with continuous reflectors (C) (Figure 12). Fractures and several bedding tops are plotted in the variable density plot in Figure 13.

The heavily-fractured zone (Area A on Figure 12) is bounded on the north by a well-defined fracture (shown by the arrow). It is called a fracture rather than a fault because it was not possible to correlate reflections across it to determine if movement had occurred. Reflection

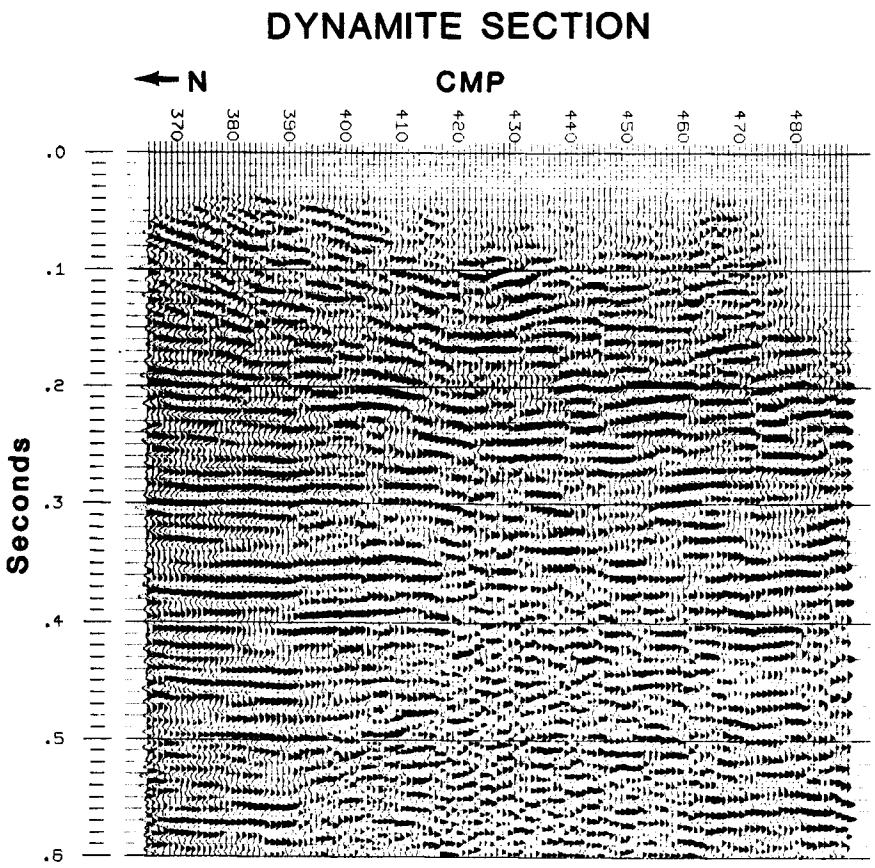

Figure 11. Seismic reflection profile for the dynamite data. Horizontal distance across the line is approximately one kilometer. Depth at 0.5 seconds is approximately one kilometer.

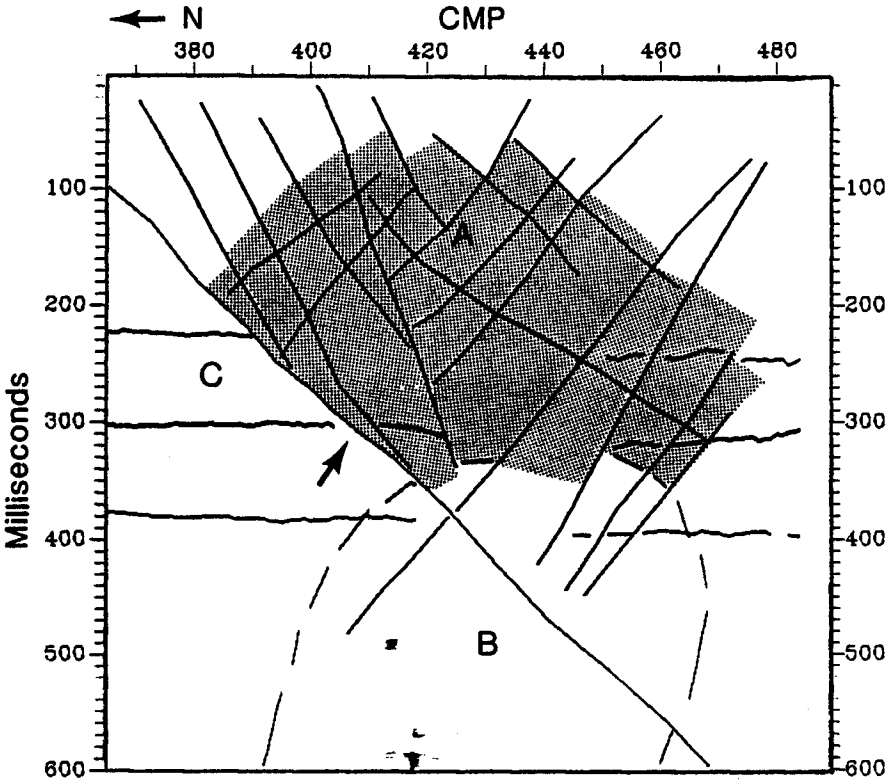

Figure 12. Interpretative line drawing for the seismic reflection profile shown in Figure 11. Shaded region is the zone of sills. Continuous lines indicate the zone of continuous reflectors. Clear region is the chaotic zone. Arrow indicates the bounding fracture. Top of the Mississippian is at approximately 0.22 seconds. Top of the Arbuckle is at approximately 0.30 seconds. Basement is at approximately 0.380 seconds.

Figure 13. Fractures and several horizons are plotted in this variable density plot. Green stripe represents the top of the Mississippian; yellow stripe represents the top of the Arbuckle; purple stripe represents the top of the basement.

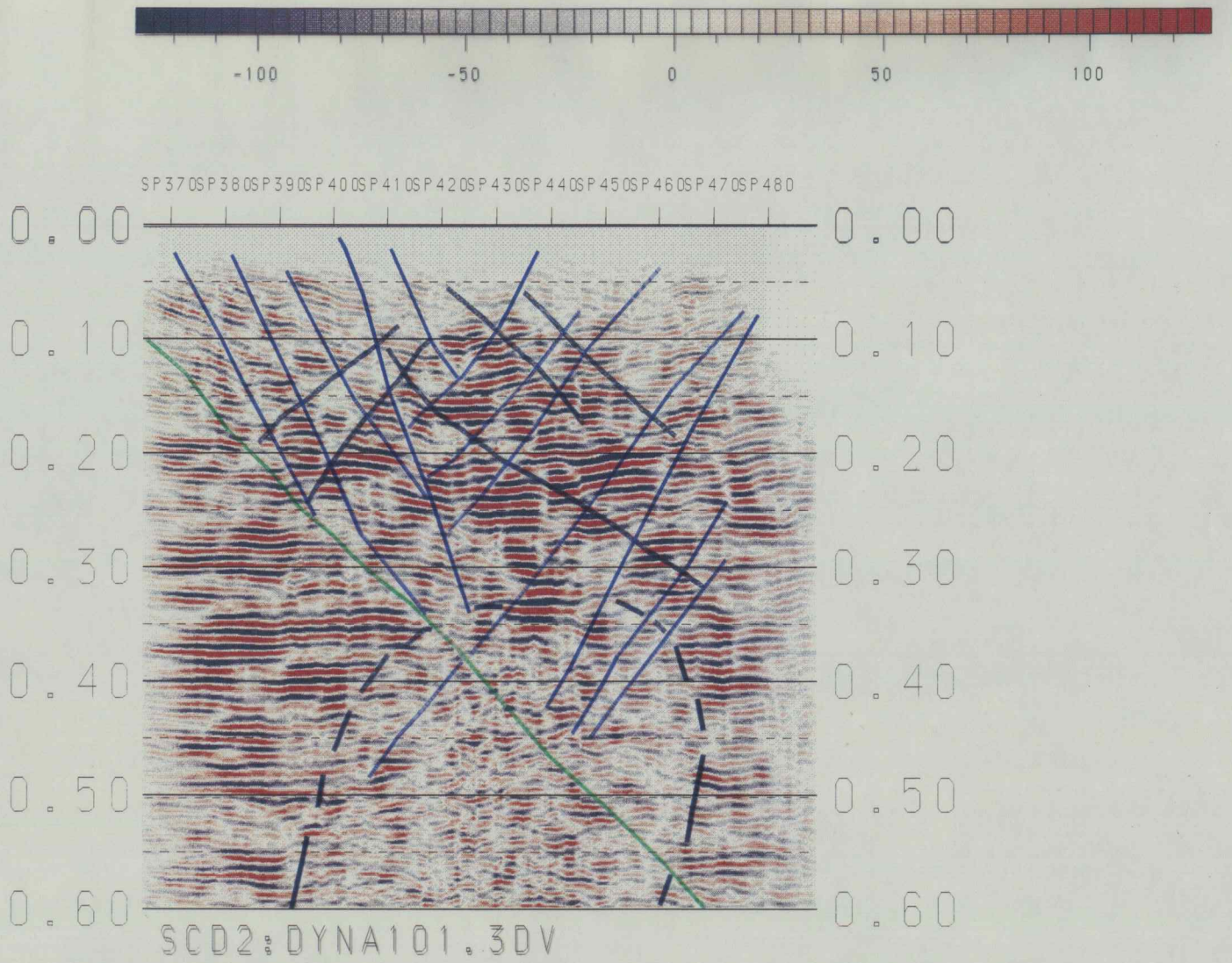
-100
-50
0
50
100
SP370SP380SP390SP400SP410SP420SP430SP440SP450SP460SP470SP480
0.00
0.10
0.20
0.30
0.40
0.50
0.60
SCD2:DYNA101.3DV

events within the fractured zone have larger amplitude and lower frequency and are more discontinuous than reflections to the left of the bounding fracture. Because of this difference in character with respect to the rest of the seismic section, this zone is interpreted to be a zone of sills interlayered with the sedimentary rocks. The sills are present at greater depths than described in literature on Silver City Dome. The deepest sill was reported by Franks (1959) to be at 230 meters depth. However, a driller's log from a well (Ecco Ranch Inc. #2 drilled by White Pine Petro. Co.) located less than one mile away on the eastern edge of the dome notes lamproite at 360 meters depth and thus supports the seismic data.

The chaotic zone (Area B on Figure 12) is located beneath the zone containing sills. Reflection events to the left and right of this zone are abruptly terminated at the boundaries. There are no continuous reflection events on the inside which appears to consist of high-frequency noise. Attempts at velocity analysis in this region were not successful. The data suggest that this region is inhomogeneous in a spatial sense. This zone could be interpreted as a region in which rocks have been fractured such as if they had been intruded by magma. Therefore, I interpret this chaotic zone to consist of igneous rock mixed with country rock.

The reflections (Area C on Figure 12) to the left of the bounding fracture appear to be unaffected by the faulting. This zone is interpreted to be underlain by the normal stratigraphic section. The log of a well one mile to the east was used to correlate stratigraphy with coherent reflected events on the seismic section. The top of the Mississippian is located at 0.22 seconds (green stripe on Figure 13) at the northern portion of the line, whereas the top of the Arbuckle is the strong reflector at 0.30 seconds (yellow stripe on Figure 13). Basement is located at 0.38 seconds (purple stripe on Figure 13).

Analysis of the black-and-white seismic section showed a potential location of a zone of sills, and as a result, provided new insight as to the location of the magma source and feeder. Color plots of the seismic amplitude intensity, instantaneous amplitude, instantaneous phase, and instantaneous frequency helped to reinforce the ideas developed from the black-and-white section.

Figures 13 and 14 are color plots of the seismic amplitude intensity. The peaks of the seismic trace were assigned red colors, whereas the troughs were assigned blue ones. The colors are graded in intensity depending on the amplitude. The overlay in Figure 14 shows the fractures within the zone of sills and an outline of the chaotic zone. The bounding fracture for the zone of sills is shown

Figure 14. In the seismic amplitude intensity plot, the peaks of the seismic trace were assigned different shades of red, while the troughs were assigned different shades of blue. The colors are graded in intensity depending on amplitude. The zone of sills is characterized by higher amplitude intensity than the rest of the section. Fractures stand out much clearer on this plot than on the black-and-white section. Bounding fracture of the zone of sills is shown in green.

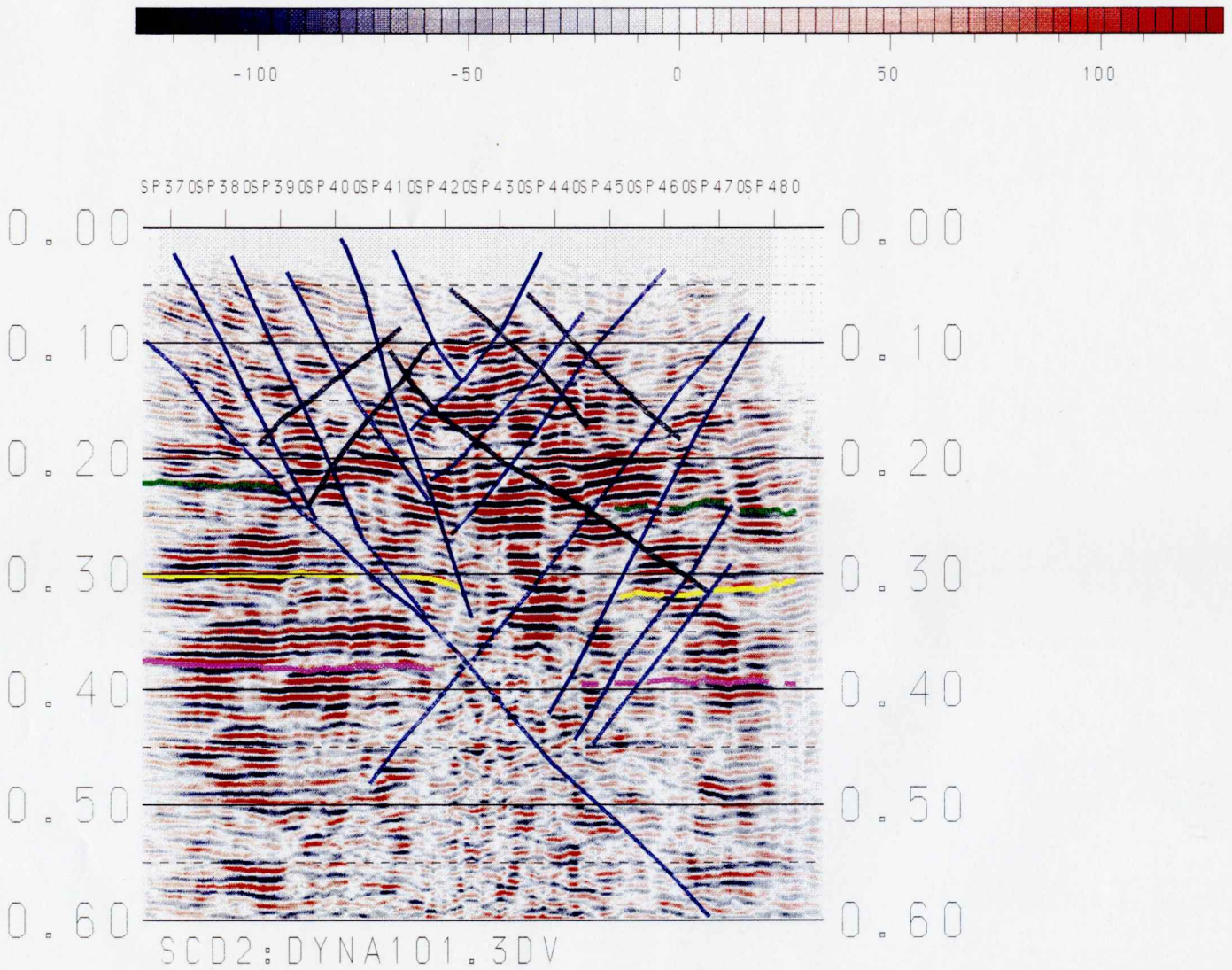
-100
-50
0
50
100
SP370SP380SP390SP400SP410SP420SP430SP440SP450SP460SP470SP480
0.00
0.10
0.20
0.30
0.40
0.50
0.60
SCD2:DYNA101.3DV

in green. The same overlay will be used in the next three color plots. The area in which the sills are believed to be located has a stronger intensity than the area thought to be undisturbed by the sills. This plot also shows, by the abrupt termination of reflections, the boundaries of the chaotic zone. In addition, the faulting within the zone of sills is more visible on the colored plot than on the black-and-white one.

Instantaneous amplitude color plots are scaled in terms of the largest amplitude which is chosen to be red. The plot in Figure 15 shows that the zone containing the sills has the largest instantaneous amplitude of all events on the section. Taner et al. (1979) state that boundaries across which major lithologic changes occur often have high reflection strength. Such a boundary could be that existing between the sedimentary rocks and the lamproite sills. The area interpreted to be normal section is of lower instantaneous amplitude as shown by the orange and yellow colors on the seismic section.

Instantaneous phase plots emphasize the continuity of events. The reason is that all amplitude information is removed and thus strong and weak events will show up equally. In Figure 16, the sills are not as distinguishable as they were on the instantaneous amplitude plot. Fractures within the zone are the features which

Figure 15. Instantaneous amplitude plots are scaled according to the largest amplitude which is chosen to be red. The zone of sills is characterized by having the highest amplitude on the section. The overlay is identical to that of Figure 14.

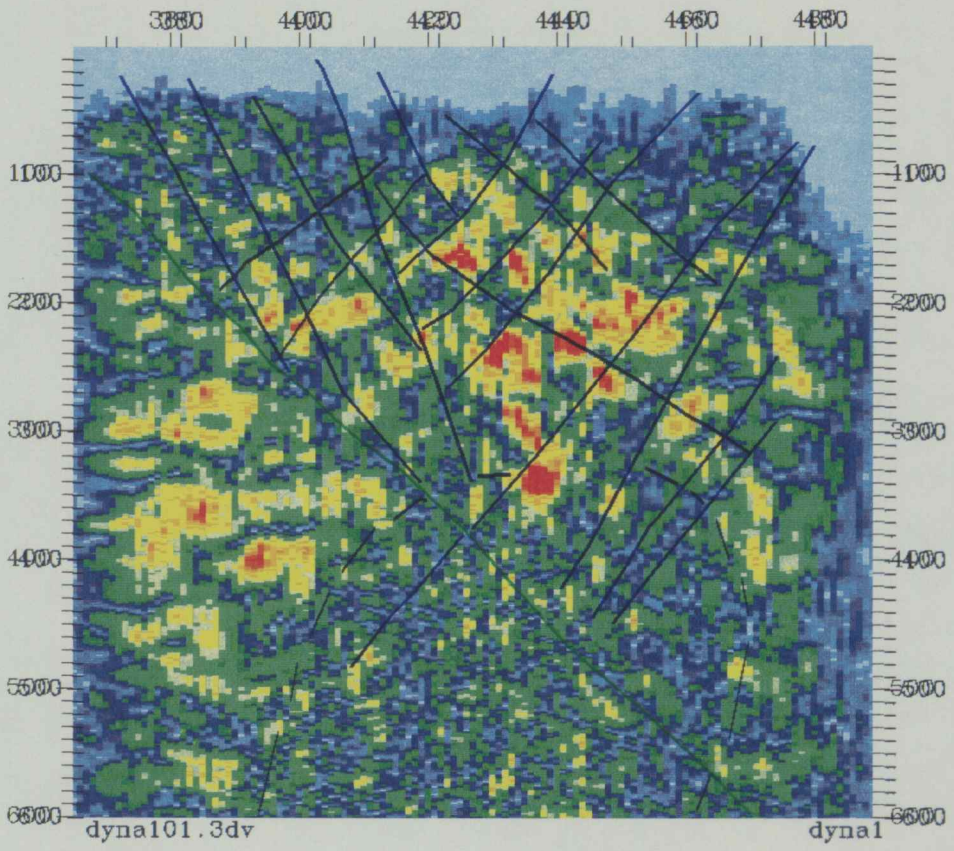
3850
4000
4220
4440
4660
4850
1000
2200
3300
4400
5500
6600
dyna101.3dv
dyna1

Figure 16. Discontinuities on the seismic sections are emphasized on the instantaneous phase plot. The overlay is identical to that of Figure 14.

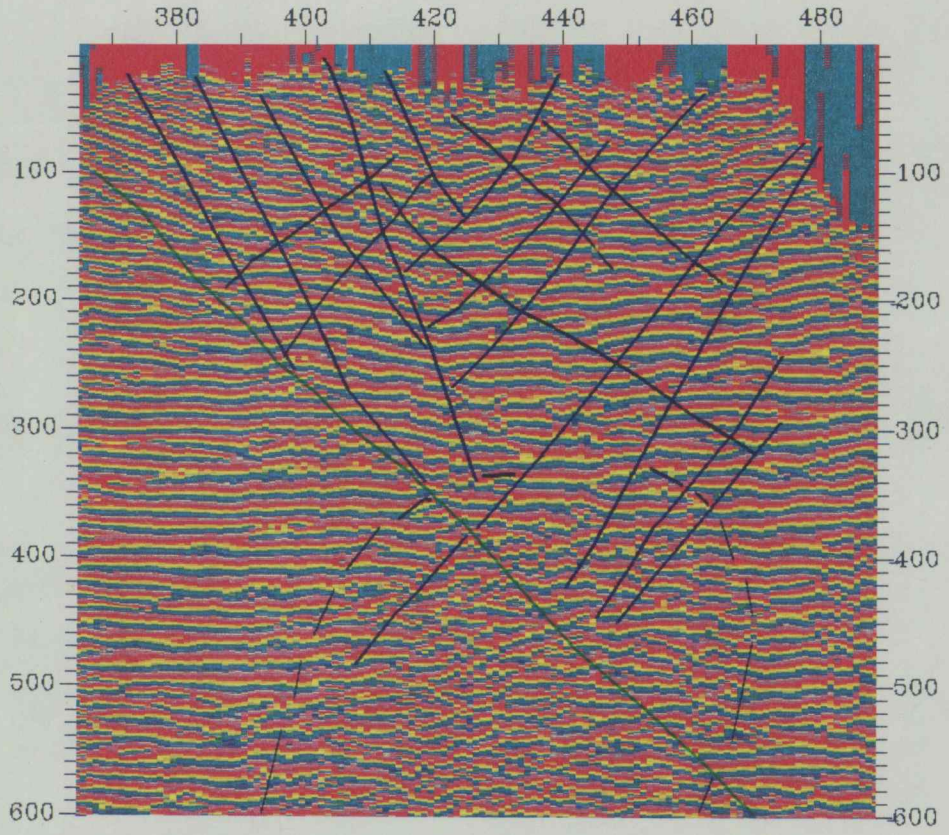
380
400
420
440
460
480
100
200
300
400
500
600

really stand out. The chaotic zone and the fracture which bounds the sill zone are much clearer on the instantaneous phase plot than they were on the black-and-white section.

The instantaneous frequency plot (Figure 17) shows by the red and yellow colors that the zone interpreted to contain sills does have lower frequencies compared with events on the same level across the bounding fracture. The fractures within the intrusion-infested zone are seen on these plots as high-frequency events shown by the blue and green colors. The chaotic zone stands out as a disorganized mixture of high and low frequencies.

The migrated seismic section for the dynamite profile is shown in Figure 18 and appears to be less contaminated with high-frequency noise than the unmigrated section of Figure 14. The bottom and sides of the section show smearing of the data which is a result of edge effects at the boundaries. The dip of the reflectors did not change noticeably after migration because their original dip was not large enough to cause distortion of the data. The migrated reflections are lower in frequency than the unmigrated reflections due to the vertical projection to lower frequencies in the transform plane (Appendix G). The dip of the fractures was increased after migration. Since the effect of migration decreases with depth, the increased fracture dip occurred only in the shallow part of the

Figure 17. The instantaneous frequency plot shows the zone of sills to contain lower frequencies compared with events on the same level outside the zone. The chaotic zone contains a mixture of high and low frequencies. The overlay is identical to that of Figure 14.

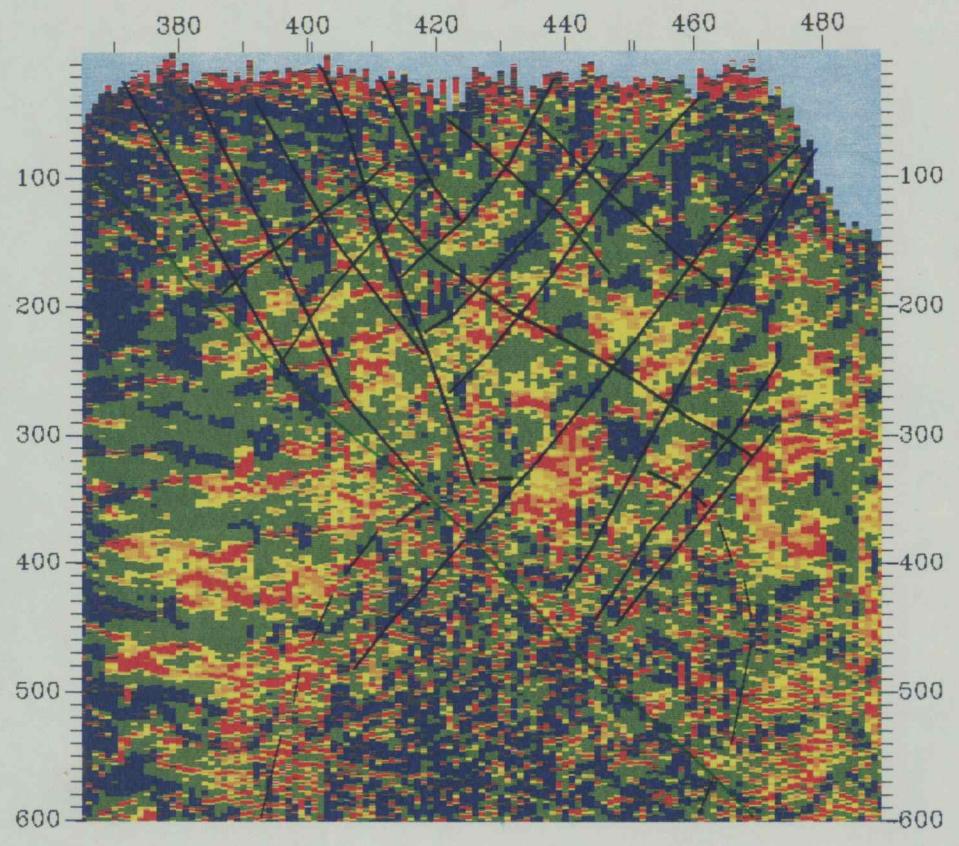
380
400
420
440
460
480
100
200
300
400
500
600

Figure 18. Seismic section after migration. Overlay shows the fractures within the zone of sills.

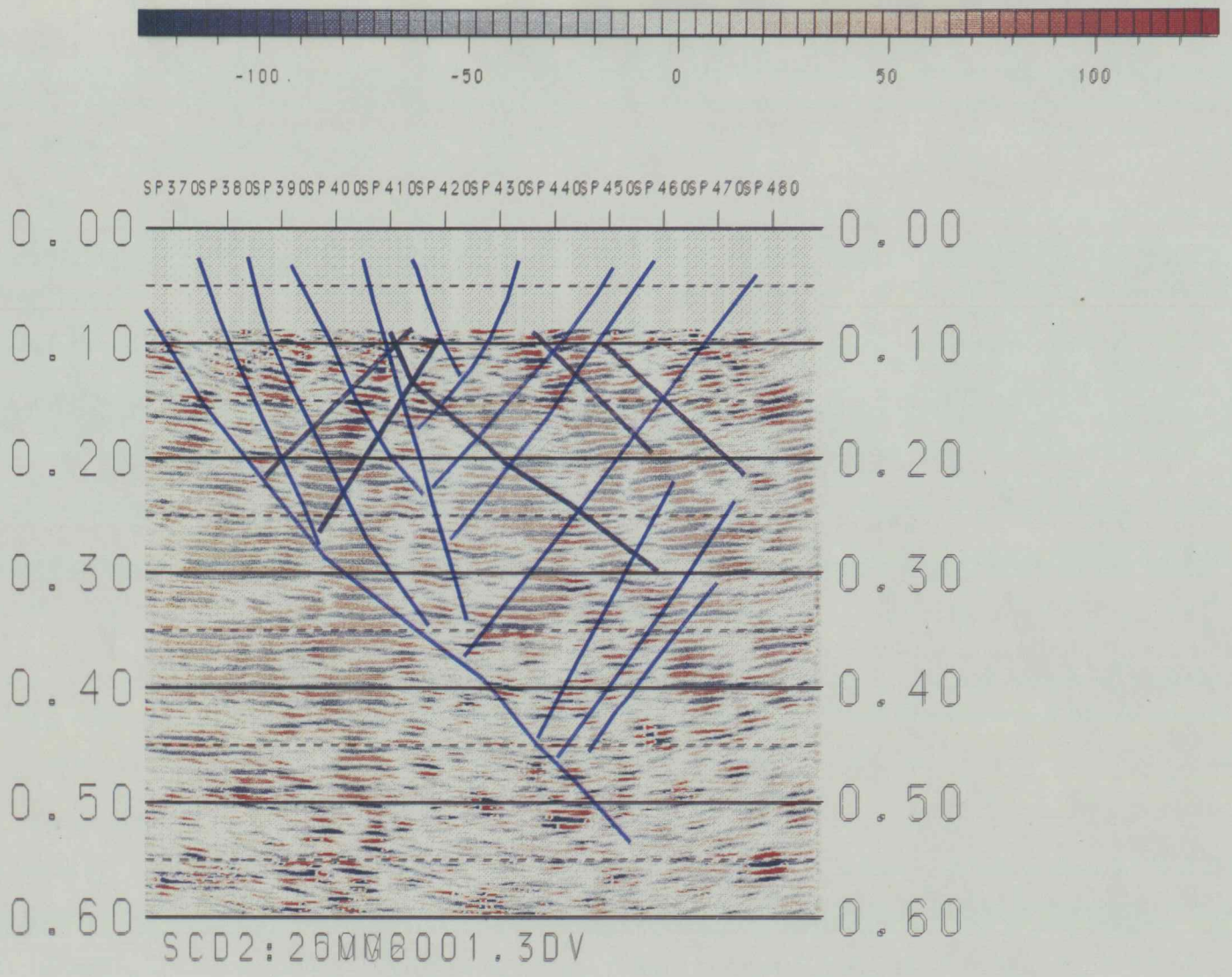
-100
-50
0
50
100
SP370SP380SP390SP400SP410SP420SP430SP440SP450SP460SP470SP480
0.00
0.10
0.20
0.30
0.40
0.50
0.60
SCD2:2000001.3DV

section. Lines have been drawn on the overlay for Figure 18 to indicate some of these fractures within the zone of sills. The zone seems to be very shattered as shown by the criss-cross pattern of fractures. The fractures can be correlated from one seismic section to another as shown by comparing Figures 14 and 18. The velocity of the stacked section varied both horizontally and vertically in the x-z domain; however, a constant velocity of 13 000 ft/sec was used to migrate the data. Using a constant velocity in migration did not appear to be a problem since the two sections correlated quite well. The small angle of dip of the relectors was probably the main reason that the constant velocity algorithm could be used successfully in this area of varying velocities. Migration aided the identification of the northern boundary of the chaotic zone on the seismic data; however, due to smearing effects from the side and bottom edges of the section, the southern boundary is not as visible as it is on the unmigrated data.

ORIGIN OF REFLECTIONS IN THE ZONE OF SILLS

Reflections come from interfaces across which there is an acoustic impedance (velocity multiplied by density) contrast. The larger the difference in acoustic impedance, the stronger the reflection. I considered two ideas to explain the origin of the strong reflections within the zone of sills. These reflections could be direct

reflections from the sills. They could also be reflections from the contact between metamorphosed and unmetamorphosed sedimentary rocks. Contact metamorphic rocks exist above and below the sills and were formed by the heat from the intrusion. Thus, the reflections could be due to the acoustic impedance contrast between metamorphosed and unmetamorphosed rocks.

To test these possibilities, I assigned velocity and density values to the lamproite and to the unmetamorphosed and metamorphosed limestones and shales and calculated the reflection coefficient for contacts between metamorphosed shale-lamproite, metamorphosed limestone-lamproite, metamorphosed shale-shale, metamorphosed limestone-limestone, metamorphosed limestone-metamorphosed shale, and limestone-shale. The larger the reflection coefficient, the stronger the reflection. First, the model shows that a reflection from the boundary between unmetamorphosed limestone and shale has a large reflection coefficient, but it is not as large as those seen in the zone of sills. This fact is demonstrated by the normal section portion of the amplitude intensity plot (Figures 13,14) and the instantaneous amplitude plot (Figure 15). A metamorphosed shale-lamproite contact shows the largest reflection coefficient. Contacts between metamorphosed limestone-limestone and metamorphosed limestone-metamorphosed shale

also have large reflection coefficients. The strong events could be produced by reflections from any of these three metamorphic contacts.

If the strong reflection events are at their maximum amplitude, then they are said to be "tuned". Under these conditions, the top and bottom of a reflector is separated by a quarter-wavelength. The quarter-wavelength-thickness, or tuning thickness, is calculated as follows:

$$d = \lambda/4 = 1/4(V/f).$$

If the reflections are directly from the sills, then their thicknesses would have to be about 6 to 11 meters to produce the large reflections observed. A thickness of 11 meters is close to their known maximum thickness.

In conclusion, the model showed that three contacts could serve as potential sources for the strong reflections within the zone of sills. I believe that one of these possibilities, the metamorphosed limestone-limestone contact, can be eliminated because I think that all the sedimentary rocks in this part of the section have been metamorphosed. Thus, I conclude that the reflections result from acoustic impedance contrasts across contacts between metamorphosed limestone-metamorphosed shale and between metamorphosed shale-lamproite.

MAGNETIC DATA

ACQUISITION

Magnetic data were collected in the northeastern portion of the dome in the vicinity of the seismic line as shown in Figure 19. Data were collected along seven north-south trending lines (lines 1-7), one of which (line 4) directly followed the seismic line. Data were also collected along three east-west-trending lines (lines 8-10) which intersected three of the north-south lines. Measurements were made at intervals of 7.5 and 15 meters along these lines. Two or three readings were taken at each station, and the average of these values was calculated to be used in processing. Readings were taken at a base station every half hour to hour. This procedure was necessary so that effects due to drift in the magnetic field and in the instrument could be removed. A proton-precession magnetometer was used to collect the data.

PROCESSING

Several anomalies were seen on the data when plotted as profiles. Sheriff (1984) defines an anomaly to be "a portion of a geophysical survey, such as a magnetic or gravity survey, which is different in appearance from the survey in general". Some of the anomalies were caused by interference from machinery at a nearby quarry. These points were removed from the data. The remaining anomalies

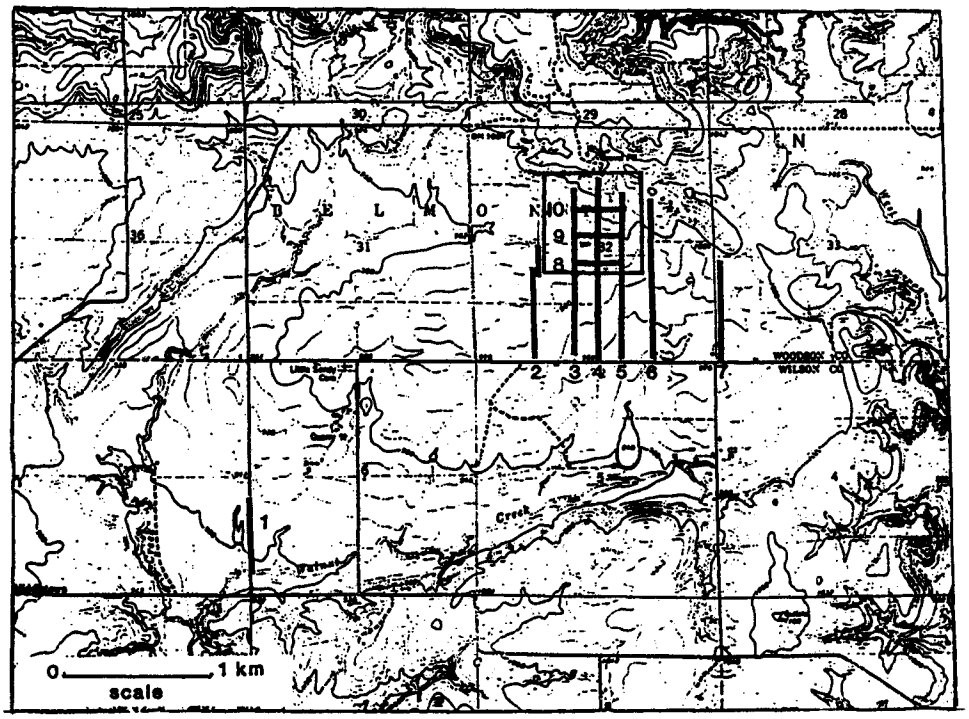

Figure 19. Topographic map of Silver City Dome showing the location of the magnetic profiles. The seismic line coincided with magnetic profile 4. Data within the square have been tied to a base.

on the profiles (Figures 20 and 21) are supported by numerous points, and since there were no power lines or fences in the immediate vicinity, these anomalies are assumed to be representative of the geology beneath the surface.

The other processing step applied to the magnetic data was drift correction. The same base station was used in the collection of lines 1,2,4,6, and 7. The rest of the data (lines 3,5,8,9,10) were collected at a different time without using a base station because it was thought that a loop closure calculation could be used to tie these data in with the data that had been drift-corrected. The data from lines 8,9, and 10 were able to be tied because these lines intersected line 4 whose data had been corrected for drift. Likewise, data from lines 3 and 5 within the square in Figure 19 were able to be drift-corrected because these lines intersected the drift-corrected east-west lines. Data from lines 3 and 5 below the square in Figure 19 were unable to be tied because these portions of the lines did not intersect any other line which had been drift-corrected. As a result, a meaningful map of all the magnetic data points could not be made. The profiles were useful in qualitative interpretation only and were used as support for the seismic data.

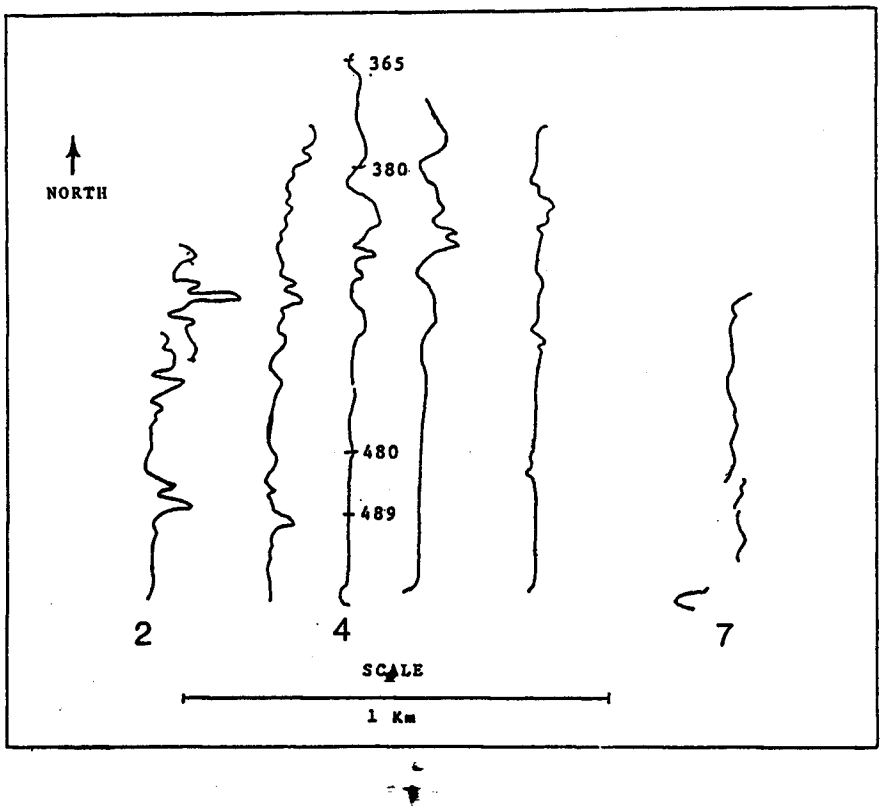

Figure 20. Magnetic profiles for 6 of the north-south-oriented magnetic lines. Anomalies on the profile of line 4 coincide with the zone of sills on the seismic data. These anomalies can be correlated to lines 2 through 6. The profile for line 1 was uneventful, so it is not displayed.

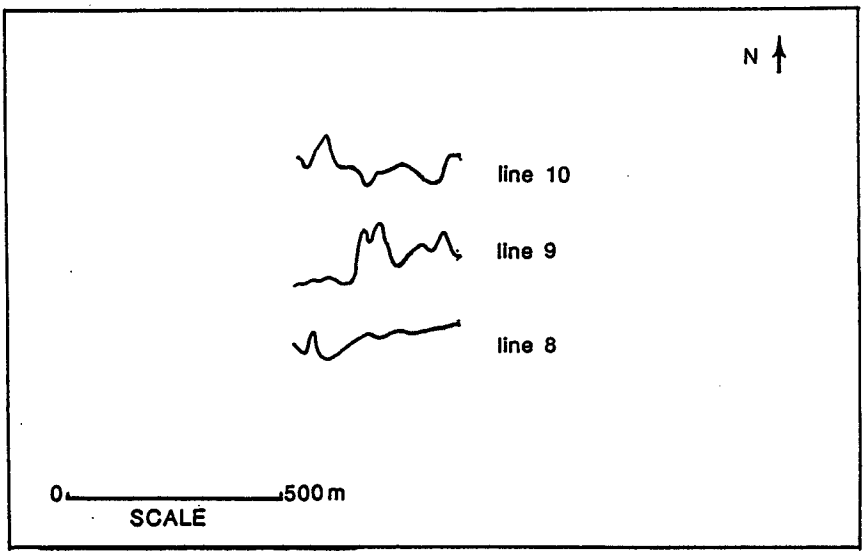

Figure 21. Three east-west magnetic profiles are displayed. The anomalies present appear to be valid as they were supported by numerous data points. All three profiles show an overall increase in magnitude to the east.

INTERPRETATION

Many fractures seen on the seismic section are not readily apparent at the surface. Fractured strata often have distinctive magnetic signatures; thus, magnetic data were collected at the dome in an attempt to recognize anomalies due to the fractures in the collapsed zone. On the magnetic profile from line 4, which was located along the path of the seismic line, an anomalous zone was present in the region of the collapsed zone seen on the seismic data. The magnetic profile from this line, as well as the profiles from the other north-south-oriented lines, are shown in Figure 20. The CMP's are labeled on the profile for Line 4 to show the correlation between the seismic and magnetic data. The collapsed zone on the seismic data is highly fractured and is located between CMP's 380 to 480. The major magnetic anomalies are also located between these points as shown on the profile. The rest of the magnetic data along line 4 appear to be quiet in comparison. The anomalous zone is present on at least six of the north-south-trending magnetic profiles and has a northeast-southwest trend. Magnetic profile 1, collected one and a half miles west and one mile south of the seismic line (Figure 19), did not show any anomalous zones at all, so it is not displayed in Figure 20. As seen on infrared and black-and-white aerial photos, most of the faults in the

area of the dome are relatively short, linear features which trend in a northeast-southwest direction. The linearly-trending anomaly in Figure 20 could represent one of these fault zones. The anomaly changes character from east to west. The magnitude of the anomaly dies out to the northeast which may indicate the end of this zone. If the anomaly does represent the fault zone, then east-west profiles such as those shown in Figure 21 could be studied to gain an idea of the character of the width of the zone. Each profile intersected lines 3, 4, and 5 (see Figure 19). All three profiles show anomalies which are supported by several data points; however, the anomalies are not easily correlated from one profile to another. The magnetic profile for Line 8 shows a gradual increase to the east with an anomaly at its western edge. This anomaly is located where Line 8 intersects the southern edge of the proposed fault zone. The magnetic profile for Line 9 was measured just south of the northern edge of the proposed fault zone and is not as quiet as the profile for Line 8 in that it contains two significant anomalies; one is at its eastern edge and one is in its center. Comparison of this profile with that of Line 8 may indicate that the southern edge of the fault zone is better defined than the northern edge. The profile for Line 10, which lies outside the collapsed zone seen on the seismic data, is very irregular

and does not seem to be part of this fault zone at all. The collapsed zone seen on the seismic data is included within the discussed fault zone. It is possible that the fault zone provided an area of weakness along which magma could easily rise.

DISCUSSION AND CONCLUSIONS

The color plots depicting the complex trace attributes of instantaneous amplitude, instantaneous phase, and instantaneous frequency reveal details on the seismic section which are only hinted at on the black and white section and thus are useful in the interpretation stage. Their most useful application is in showing the boundaries of the chaotic zone and showing the fractures. Prior to the application of complex trace analysis, the application of data-processing techniques such as refraction statics and slant stack (Appendices D and E) successfully brought out the signal relative to the noise. The frequency-wave number migration technique with the constant velocity algorithm of Stolt was also applied to the data to reposition reflectors to their correct spatial locations. This resulted in a seismic section which contained less noise and which supported the interpretation obtained from the unmigrated seismic section. The final result is a seismic section (Figure 11) whose interpretation, along with the 1985 data, revises some of the previous ideas on

the formation of Silver City Dome. Wagner's interpretation of the formation of Silver City Dome was that magma intruded the Phanerozoic sedimentary section along a fault described only as dipping steeply to the north. It then penetrated laterally as sills into the Upper Pennsylvanian sedimentary rocks.

From interpretation of the seismic data collected in 1985, Krzysztof Wojcik suggested that deep-seated magmatic activity caused gentle doming in the area and subsequent formation of the marginal grabens. Additional magmatic intrusion caused sill injection and the formation of a smaller dome located in the northern portion of the larger dome. The data collected with a dynamite source shows this area of the dome in greater detail than was seen on the MiniSOSIE section. A seismically-chaotic zone is interpreted to be the feeder through which magma penetrated the overlying rock units. This zone is believed to consist of shattered country rock mixed with igneous rock which came up from deep within the earth. This feeder zone is farther toward the center of the dome than proposed by Wagner (1954). Magma intruded the overlying sedimentary section and spread between the alternating limestone and shale layers of the Pennsylvanian cyclothems. The sills interlayered with the metamorphosed sedimentary rocks produce a seismic reflection signal that is lower in

frequency and higher in amplitude than the signal from sedimentary layers alone. The fractures present in the zone containing sills are probably the result of sill penetration as well as collapse after cooling. A fracture which extends down to the chaotic zone bounds the sills on the north and possibly acted as a conduit for magma intrusion.

The magnetic data were used in a qualitative sense as support for the seismic data. A close-up of the relationship between the magnetic profile from line 4 and the seismic profile is shown in Figure 22. The pattern of anomalies could be a combination of two factors. The largest anomalies occur over the chaotic zone and the bounding fracture, suggesting that the presence of the anomalies is related to the amount of lamproite present in the rocks. Moreover, fracturing is more complex in this region. Thus, the anomalies could represent lamproite which has been fractured and probably faulted as well. The southern portion of the magnetic profile begins to level off beyond the boundary of the chaotic zone where less fracturing has occurred, and the lamproite is present only as sills.

Finally, the seismic section contains reflections within the basement which appear to represent layers. These are similar in character to the reflections in the

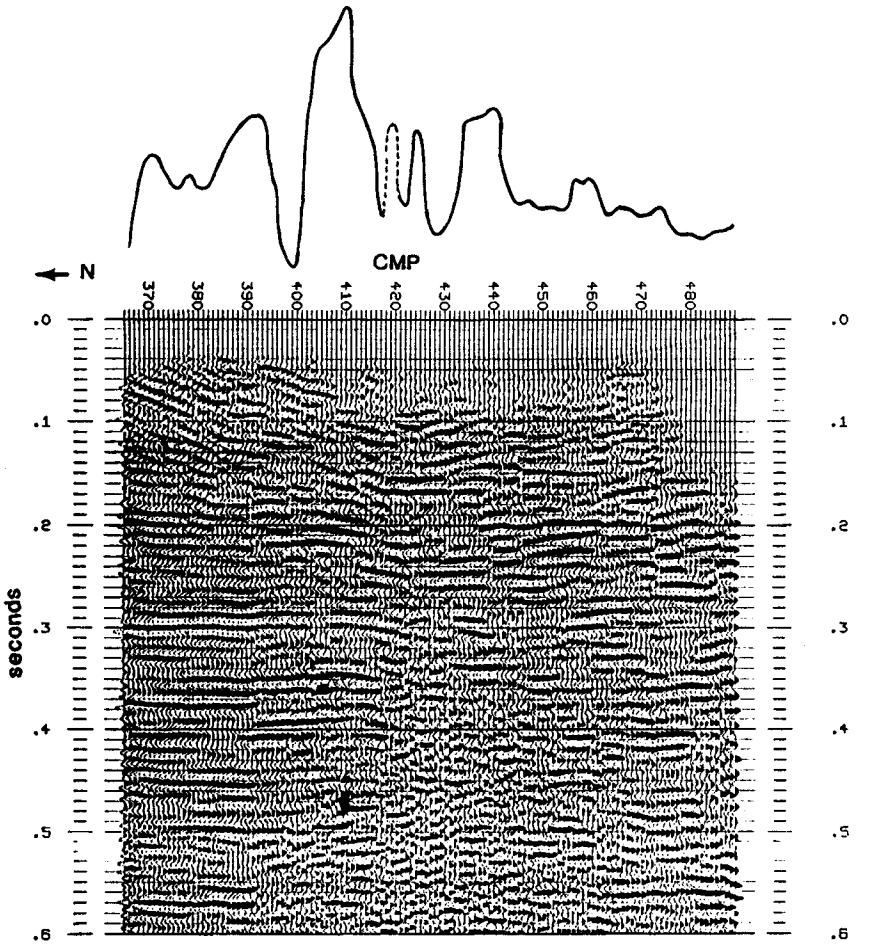

Figure 22. Comparison between the magnetic profile from line 4 and the seismic section. Magnitude of the anomalies on the magnetic data appears to increase to the north over the lamproite feeder and the zone of complex faulting. Distance across the profile is approximately one kilometer. Dashed lines represent inferred points.

sedimentary section, but their origin is unknown. They are not thought to be artifacts of processing because they do not occur across the entire seismic section. Instead, they are located to either side of the chaotic zone. Because of the difference in rock type, it is reasonable to expect that the acoustic impedance contrast within a section of granite should not be the same as that within a layered sequence of limestone, shale, and sandstone. Therefore, the seismic response of the basement should differ from that of the overlying sedimentary section. However, when looking at the seismic data alone, the boundary between the basement and the sedimentary section is not immediately apparent. This fact, plus the similarity in character of the basement reflectors to the overlying reflections, indicates that the basement events could be multiples which were generated within the overlying cyclothems. The large acoustic impedance contrast between the sedimentary layers gives rise to a strong signal; however, the layering also is a good source for multiples. Reflections within basement rocks have been the object of study by COCORP (Consortium for Continental Reflection Profiling) in areas such as the Southern Oklahoma Aulacogen (Brewer et al., 1983; Brewer, 1982; Brewer et al., 1981), the Blue Ridge and Piedmont (Cook et al., 1979), Hardemann County, Texas (Lynn et al., 1981), the Michigan Basin (Brown et al.,

1982), and northeastern Kansas (Brown et al., 1983). The layering of the basement rocks south of the Wichita Mountains has been attributed to a Proterozoic basin thought to be 1200 to 1400 million years old. Brewer et al. (1981) suggest that the layering is the result of deposition of clastic sedimentary rocks and felsic volcanic rocks in a trough which formed during a period of extension. The data show what appear to be angular unconformities and onlap and downlap relationships which suggest that depositional processes were responsible for the presence of these layered rocks. Lynn et al. (1981) interpreted the same sequence of rocks, as well as two Mesozoic batholiths in California and Nevada, to be the result of cumulate layers of igneous rocks formed due to crustal melting by mantle basalt. Brown et al. (1983) and Serpa et al. (1984) interpreted data from a seismic line collected across the Nemaha Ridge and the Midcontinent Geophysical Anomaly (MGA) in northeastern Kansas to correspond to a rift basin at the southern end of the Keeweenawan Rift. The seismic response of the basement is characterized by two distinct zones. The shallower zone consists of weak and discontinuous reflections which may be a zone consisting of sandstones and conglomerates. Beneath this layer is a zone of high-amplitude reflections and diffractions which may be interlayered basalts and clastic

rocks. These units can be correlated to the northern part of the rift. Smithson et al. (1979) studied data from the Wind River Uplift in Wyoming and concluded that the reflections from the basement were multiples from the overlying sedimentary rocks because there was no change in reflection character across the basement reflector. The use of one-dimensional models demonstrated that multiple reflections could be strong enough to interfere with the basement reflectors (Zawislak and Smithson, 1981).

REFERENCES

Barry, K.M., Cavers, D.A., and Kneale, C.W., 1975, Recommended standards for digital tape formats: Geophysics, **40**, 344-352.

Bergman, 1987, Lamproites and other potassium-rich igneous rocks: a review of their occurrence, mineralogy and geochemistry: in Fitton, J.G. and Upton, B.G.J., Eds., Alkaline igneous rocks: Geological Society Special Publication **30**, Blackwell Scientific Publications, 103-190.

Bickford, M.E., Harrower, K.L., Hoppe, W.J., Nelson, B.K., Nusbaum, R.L., and Thomas, J.J., 1981, Rb-Sr and U-Pb geochronology and distribution of rock types in the Precambrian basement of Missouri and Kansas: Geol. Soc. Am. Bulletin, **92**, 323-341.

Bickford, M.E., Mose, D.G., Wetherill, G.W., and Franks, P.C., 1971, Metamorphism of Precambrian granite xenoliths in a mica peridotite at Rose Dome, Woodson County Kansas: Part 1, Rb-Sr isotopic studies: Geol. Soc. Am. Bulletin, **82**,2863-2868.

Bracewell, R.N., 1965, The Fourier transform and its applications: McGraw-Hill Book Co., Inc., San Francisco, 444 p.

Brewer, J.A., 1982, Study of southern Oklahoma Aulacogen using COCORP deep seismic-reflection profiles: in Gilbert, M.C., Donovan, R.N., Eds., Geology of the eastern Wichita Mountains, southwestern Oklahoma: Oklahoma Geological Survey Guidebook **21**, University of Oklahoma Printing Services, 31-39.

Brewer, J.A., Good, R., Oliver, J.E., Brown, L.D., and Kaufman, S., 1983, COCORP profiling across the Southern Oklahoma aulacogen: Overthrusting of the Wichita Mountains and compression within the Anadarko Basin: Geology, **11**, 109-114.

Brewer, J.A., Brown, L.D., Steiner, D., Oliver, J.E., Kaufman, S., and Denison, R.E., 1981, A proterozoic basin in the southern midcontinent of the United States revealed by COCORP deep seismic reflection profiling: Geology, **9**, 569-575.

Brown, L., Jensen, L., Oliver, J., Kaufman, S., and Steiner, D., 1982, Rift structure beneath the Michigan Basin from COCORP profiling: Geology, **10**, 645-649.

Brown, L., Serpa, L., Setzer, T., Oliver, J., Kaufman, S., Lillie, R., Steiner, D., and Steeples, D.W., 1983, Intracrustal complexity in the United States midcontinent: Preliminary results from COCORP surveys in northeastern Kansas: Geology, **11**, 25-30.

Chun, J.H., and Jacewitz, C.A., 1981, Fundamentals of frequency domain migration: Geophysics, **46**, 717-733.

Claerbout, J.F., 1985, Imaging the earth's interior: Blackwell Scientific Publications, Boston, 398 p.

Cook, F.A., Albaugh, D.S., Brown, L.D., Kaufman, S., Oliver, J.E., and Hatcher, Jr., R.D., 1979, Thin-skinned tectonics in the crystalline Southern Appalachians: COCORP seismic-reflection-profiling of the Blue Ridge and Piedmont: Geology, **7**, 563-567.

Cullers, R.L., Ramakrishnan, S., Berendsen, P., and Griffin, T., 1985, Geochemistry and petrogenesis of lamproites, late Cretaceous age, Woodson County, Kansas, U.S.A.: Geochim. Cosmochim. Acta. **49**, 1388-1402.

Farrell, R.C., and Euwema, R.N., 1984, Refraction statics: Proc. IEEE, **72**, 1316-1329.

Franks, P.C., 1959, Pectolite in mica peridotite, Woodson County, Kansas: Am. Mineral., **44**, 831-850.

Franks, P.C., Bickford, M.E., and Wagner, H.C., 1971, Metamorphism of Precambrian granitic xenoliths in a mica peridotite at Rose Dome, Woodson County, Kansas: Part 2, Petrologic and mineralogic studies: Geol. Soc. Am. Bulletin, **82**, 2869-2890.

Hambleton, W.W., and Merriam, D.F., 1955, Magnetic anomalies in Woodson and Wilson Counties, Kansas: Kansas Geol. Survey Bull. **114**, 113-128.

Heckel, P.H., 1978, Guidebook to Upper Pennsylvanian cyclothemic limestone facies in eastern Ks.: Kansas Geological Survey, The University of Kansas, 79 p.

Heckel, P.H., 1977, Origin of phosphatic black shale facies in Pennsylvanian cyclothems of Midcontinent North America: Bull. Am. Assn. Petr. Geol., **61**, 1045-1068.

Knapp, R.W., and Steeples, D.W., 1986, High-resolution common-depth-point reflection profiling: Field acquisition parameter design: Geophysics, **51**, 283-294.

Knapp, R.W., Markezich, M.A., Wojcik, K.M., 1988, Seismic reflection studies at Silver City Dome, Kansas (abstract): 22nd annual South-Central Section, abstracts with programs, Geol. Soc. Am., **20**, 104.

Lynn, H.B., Hale, C.D., and Thompson, G.A., 1981, Seismic reflections from the basal contacts of batholiths: J. Geophys. Res., **86**, 10633-10638.

Merriam, D.F., 1963, The geologic history of Kansas: Kansas Geological Survey Bulletin, **162**, 1-317.

Merrill, R.B., Bickford, M.E., and Irving, A.J., 1977, The Hills Pond Peridotite, Woodson County, Ks.: A richterite-bearing Cretaceous intrusive with kimberlitic affinities (Ext. Abstract): 2nd Kimberlite Conf. Santa Fe, New Mexico, 3 p.

Oliver, J.E., 1978, Exploration of the continental basement by seismic reflection profiling: Nature, **275**, 485-488.

Paul, R.W., 1970, The age and origin of the Decaturville structure, Camden and Lacledes Counties, Missouri: Master's Thesis, The University of Kansas, 38 p.

Schilt, F.S., Kaufman, S., and Long, G.H., 1981, A three-dimensional study of seismic diffraction patterns from deep basement sources: Geophysics, **46**, 1673-1683.

Serpa, L., Setzer, T., Farmer, H., Brown, L., Oliver, J., Kaufman, S., and Sharp, J., 1984, Structure of the southern Keeweenawan Rift from COCORP surveys across the midcontinent geophysical anomaly in northeastern Kansas: Tectonics, **3**, 367-384.

Sheriff, R.E., 1984, Encyclopedic dictionary of exploration geophysics: Society of Exploration geophysicists, Tulsa, 323 p.

Sheriff, R.E., 1980, Seismic stratigraphy: International Human Resources Development Corp., Boston, 227 p.

Sheriff, R.E., and Geldart, L.P., 1983, Exploration Seismology, volume 2- Data-processing and interpretation: Cambridge University Press, 221 p.

Smithson, S.B., Brewer, J.A., Kaufman, S., Oliver, J.E., and Hurich, C.A., 1979, Structure of the Laramide Wind River uplift, Wyoming, from COCORP deep reflection data and from gravity data: J. Geophys. Res., **84**, 5955-5972.

Snyder, F.G., and Gerdemann, P.E., 1965, Explosive igneous activity along an Illinois-Missouri-Kansas axis: Am. J. Science, **263**, 465-493.

Stoffa, P.L., Buhl, P., Diebold, J.B., and Wenzel, F., Direct mapping of seismic data to the domain of intercept time and ray parameter - A plane wave decomposition: Geophysics, **46**, 255-267.

Taner, M.T., and Koehler, F., 1981, Surface consistent corrections: Geophysics, **46**, 17-22.

Taner, M.T., and Sheriff, R.E., 1977, Application of amplitude, frequency, and other attributes to stratigraphic and hydrocarbon determination: in Payton, C.E., Ed., Applications to hydrocarbon exploration: AAPG Memoir **26**, Am. Assn. Petroleum Geologists, 301-327.

Taner, M.T., Koehler, F., and Sheriff, R.E., 1979, Complex seismic trace analysis: Geophysics, **44**, 1041-1063.

Tatham, R.H., 1984, Multidimensional filtering of seismic data: Proc. IEEE, **72**, 1357-1369.

Tatham, R.H., Keeney, J.W., and Noponen, I., 1983, Application of the tau-p transform (slant stack) in processing seismic reflection data: Bull. Austr. Soc. Explor. Geophys., **14**, 163-172.

Twenhofel, W.H., 1917, Granite boulders in (?) the Pennsylvanian strata of Kansas: Am. J. Science, **43**, 363-380.

Twenhofel, W.H., 1919, Additional facts relating to the granite boulders of southeastern Kansas: Am. J. Science, **48**, 132-135.

Twenhofel, W.H., 1926, Intrusive granite of the Rose Dome, Woodson County, Kansas: Geol. Soc. Am. Bulletin, **37**, 403-412.

Wagner, H.C., 1954, Geology of the Fredonia Quadrangle, Kansas: U.S. Geol. Surv. Map, GQ49.

Wojcik, K.M., 1986, Seismic reflection study of a lamproite intrusion, Silver City Dome, Woodson County, Kansas: Kansas Geological Survey open file report, **86-26**, 21 p.

Wojcik, K.M., Berendsen, P., and Knapp, R.W., 1987, Seismic reflection study of a lamproite intrusion, Silver City Dome, Woodson Co. Ks.: Geol. Soc. Am., abstracts with programs, **18**, 793.

Yilmaz, O., 1987, Seismic data processing: Society of Exploration Geophysicists, Tulsa, 526 p.

Zartman, R.E., Brock, M.R., Heyl, A.V., and Thomas, H.H., 1967, K-Ar and Rb-Sr ages of some alkalic intrusive rocks from central and eastern United States: Am. J. Science, **265**, 848-870.

Zawislak, R.L., and Smithson, S.B., 1981, Problems and interpretation of COCORP deep seismic reflection data, Wind River range, Wyoming: Geophysics, **46**, 1684-1701.

Zeller, D.E., Ed., 1968, The stratigraphic succession in Kansas: Kansas Geological Survey Bulletin , **162**, 317 p.

APPENDIX A

CHARACTERISTICS OF LAMPROITES
(From Bergman, 1987)

1. Major mineral content (>5-10%)- titanium phlogopite (Al-depleted), clinopyroxene (Al-depleted diopside), alkali amphibole (usually Al-depleted K-Ti-richterite), olivine, leucite (Na-poor, Fe-rich), and sanidine (Fe-rich).

2. Accessory minerals (<5-10%)- spinel (intermediate Cr-Mg-Fe-Al-Ti compositions), ilmenite, priderite, wadeite, shcherbakovite, jeppeite, apatite, perovskite, sphene, TiO_2 polymorphs, and rarely, enstatite.

3. Alteration products- analcite, chlorite, silica, carbonate, nontronite and other zeolites, serpentine, barite, albite, clay minerals.

4. Mineral paragenesis- Lamproites do not contain the following minerals: primary plagioclase, melilite or monticellite, kalsilite, nepheline, sodalite, nosean, hauyne, melanite.

APPENDIX B

DATA ACQUISITION PARAMETERS

Recording:	I/O DHR 2400 24-channel recording system
Source:	Dynamite
Source Spacing:	55 ft
Receivers:	30 Hz geophones, linear grouping, 55-ft long, 10 per group
Receiver Spacing:	55 ft, near offset-165 ft. far offset-1580 ft.
Geometry:	End-on
Record Length:	1000 ms
Sample Rate:	1 ms
Filters:	Low-cut 110 Hz High-cut 250 Hz Notch 60 Hz

APPENDIX C

PROCESSING PARAMETERS

DECONVOLUTION: auto-prediction,
2nd zero crossing,
operator length 30 ms

FILTERS: bandpass, length 125 ms,
0 percent points 40 and 240 Hz
100 percent points 80 and 160 Hz

SCALE: automatic gain control;
operator length 200 ms in plot

SORT: CDP gather

STATICS: refraction, automatic, and
residual

STACKING VELOCITIES:

CDP	TIME	VELOCITY (ft/sec)
365	35	13320
	210	10840
	380	11720
385	35	13320
	130	13000
	290	10810
	385	11020
396	65	9890
	150	10240
	375	11240
415	65	9890
	100	11420
435	65	9730
	90	10240
	150	10810
	165	11020
453	65	9570
	110	10420
	150	10810
460	95	10240
	150	11240

APPENDIX D

REFRACTION STATICS

Field files showed statics problems as well as noise with frequencies of the same order as the reflections. The sources for the noise included groundroll, the air-coupled wave, and machine noise from the nearby Microlite mine. Initial attempts to apply automatic statics were not successful because of the noise which was difficult to separate from the reflection signal. To aid in correcting this problem, surface-consistent statics corrections, based on refraction first breaks rather than the reflection data, were calculated and applied to the data. In surface-consistent corrections, it is assumed that the statics correction for particular surface positions, such as source and receiver positions, is constant despite the wave path (Taner and Koehler, 1981).

The purpose of statics corrections is to make the data look as if they were recorded on a horizontal surface without the presence of near-surface, low-velocity materials. If the weathering layer varies in thickness or velocity or both throughout the extent of the seismic line, then these variations will cause arrival-time differences between traces of the CDP gathers. When the data are stacked, these differences will destroy the continuity of reflection events. One way to improve such data is the

application of refraction statics which is a type of statics correction based on the arrival times of refraction events. These events contain enough information on the near-surface layers of the earth so that accurate statics corrections can be calculated. If refraction statics are applied to field files, then additional statics corrections will be lessened in magnitude (Farrell and Euwema, 1984).

The following procedure was used for the computation of refraction statics. The refraction velocity was calculated, and the first-break data were time-shifted to an approximately level position. Times for the first breaks were then hand-picked, and any residual slope across the common source positions was removed using a least-squares linear fit. The resulting intercept value was used as the initial shot statics estimate and was subtracted from the first-break picks. The initial receiver statics estimate was calculated by averaging the shot-corrected values along common receivers. After subtracting this value from the shot-corrected values, a second source statics correction was obtained by taking the average along common sources. One additional iteration for the receivers was calculated to obtain the final surface-consistent corrections. The statics corrections applied to the data can be found in Tables 1-3, and a flowchart of the

procedure is found in Table 4. As shown by Figure 23, the application of refraction statics did improve the data.

APPENDIX D (continued)

REFRACTION STATICS CORRECTIONS

Table 1
A. 1986a source pulling receivers

SHOT	SHOT CORRECTION(ms)	RECEIVER	RECEIVER CORRECTION(ms)
188	-5.2	177	3.2
189	-1.9	178	-0.8
190	-1.8	179	-1.1
191	-2.7	180	0.2
192	-2.0	181	1.0
194	-1.1	182	-0.8
195	1.3	183	-1.1
196	1.9	184	-1.1
197	2.8	185	-1.2
198	-0.6	186	-0.1
199	3.1	187	-0.4
200	2.6	188	0.9
201	2.0	189	0.2
202	-0.8	190	1.2
203	1.5	191	0.1
204	1.8	192	-0.7
205	-3.3	193	-0.3
206	-2.9	194	1.3
207	-3.8	195	1.1
208	-4.0	196	0.4
209	-3.0	197	0.6
210	-4.0	198	0.6
211	-4.5	199	0.1
212	-8.9	200	0.2
213	-16.7	201	-0.2
214	-5.8	202	-0.1
		203	-0.7
		204	-1.1
		205	-1.5
		206	-1.3
		207	-0.6
		208	0.8

APPENDIX D (continued)

Table 2
B. 1986b source pushing receivers

SHOT	SHOT CORRECTION(ms)	RECEIVER	RECEIVER CORRECTION(ms)
205	-7.0	211	0.5
206	-4.4	212	-0.3
207	-0.6	213	-0.7
208	-5.9	215	-0.6
209	-8.8	216	-0.3
210	-0.8	217	-0.2
211	4.9	218	-0.4
212	3.0	219	1.4
213	5.7	220	1.4
214	5.5	221	1.5
215	1.7	222	0.6
217	3.9	223	0.1
218	-2.4	224	-1.4
219	-3.7	225	-1.0
220	-0.7	226	-0.9
221	1.6	227	-0.5
222	-0.2	228	0.1
223	-1.2	229	-0.7
224	-1.3	230	0.2
225	0.3	231	0.3
226	-3.4	232	0.4
227	-1.2	233	-0.7
228	1.4	234	-0.9
229	1.4	235	-0.8
230	1.9	236	0.0
231	2.2	237	0.5
232	3.0	238	0.4
233	0.0	239	0.8
		240	1.2
		241	1.1
		242	0.6
		243	0.2
		244	0.0
		245	0.2
		246	0.1
		247	-0.4
		248	-0.6
		249	-1.2
		250	-1.5
		251	-1.2
		252	0.2
		254	0.0
		255	1.7
		256	1.0

APPENDIX D (continued)

Table 3
C. 1987

SHOT	SHOT CORRECTION(ms)	RECEIVER	RECEIVER CORRECTION(ms)
214	-3.5	187	-0.3
215	0.7	188	-1.5
216	0.1	189	-0.8
217	4.8	190	0.3
218	3.9	191	0.5
219	3.1	192	-0.4
220	9.3	193	0.5
221	-4.1	194	1.3
222	-1.1	195	-0.3
223	0.7	196	1.7
224	5.2	197	3.6
225	4.3	199	1.5
226	6.2	200	1.1
227	6.7	201	1.1
228	-0.9	202	-0.2
229	2.7	203	-0.6
230	-0.5	204	-4.2
231	-0.5	205	-3.6
		207	-2.7
		208	-3.3
		209	-1.5
		210	2.3
		211	2.4
		212	3.2
		213	3.3
		214	3.1
		215	2.7
		216	3.3
		217	2.4
		218	2.5
		219	1.0
		220	1.0
		221	-0.1
		222	-0.7
		223	-0.5
		224	0.4
		225	0.3
		226	0.1

APPENDIX D (continued)

Table 4

Refrection Statics Flow Chart

The flow chart on the following page is a very generalized version of the refraction statics procedure. The first-break data were set up in a two-dimensional array with common receiver values as columns and common shot values as rows. A shot correction was calculated for each shot, and a receiver correction was calculated for each receiver. The flow chart shows that two iterations for both sources and receivers were calculated to obtain the final refraction statics corrections.

The following abbreviations are used in the flow chart:

FB = FIRST BREAKS
SSE = SHOT STATICS ESTIMATE
SC = SHOT-CORRECTED VALUE
RSE = RECEIVER STATICS ESTIMATE
RC = RECEIVER-CORRECTED VALUE

The data were adjusted according to the final values, SC2 and RC2.

APPENDIX D (continued)

Table 4

FIELD FILES

CALCULATE REFRACTION VELOCITY TO TIME-SHIFT DATA TO LEVEL POSITION

PICK FIRST BREAKS (FB)

USING LEAST-SQUARES LINEAR FIT, REMOVE RESIDUAL SLOPE

SHOT STATICS ESTIMATE 1 (SSE1) = INTERCEPT FROM LEAST SQUARES ANALYSIS

SHOT-CORRECTED VALUE 1 (SC1) = FB - SSE1

RECEIVER STATICS ESTIMATE 1 (RSE1) = AVERAGE OF SC1 ALONG COMMON RECEIVERS

RECEIVER-CORRECTED VALUE 1 = SC1 - RSE1

SSE2 = AVERAGE OF RC1 ALONG COMMON SOURCES

SC2 = RC1 - SSE2

RSE2 = AVERAGE 0F SC2 ALONG COMMON RECEIVERS

RC2 = SC2 - RSE2

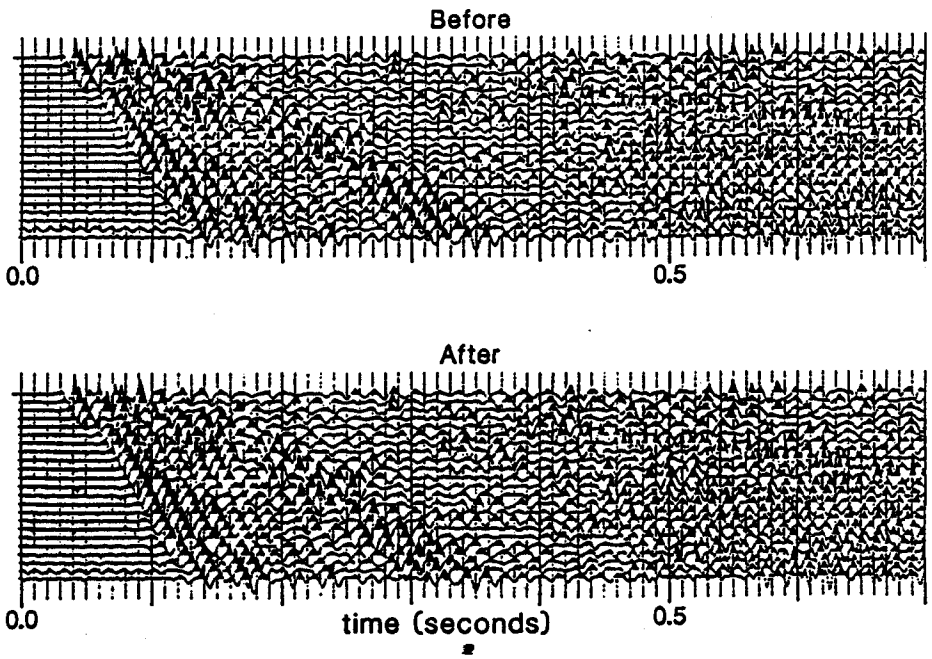

Figure 23. Application of refraction statics to the field files removed some of the statics problems. Note the improvement in data alignment which is especially evident between 0.10 and 0.15 seconds. The break in the section between traces 5 and 6 represents the omission of a bad trace from this field file.

APPENDIX E

SLANT STACK VELOCITY FILTERING

Slant stack, also called the tau-p transform, was applied as a velocity filter in order to separate signal from noise. With the application of slant stack, data are transformed from distance-time space into tau-p space in which tau is zero-offset reflection time, and p is the ray parameter or the slope of the arriving event (Tatham, 1984, Tatham, et al., 1982). The term, p, is also the inverse of the apparent horizontal velocity which is the phase velocity at which a wavefront seems to move along a line of geophones (Sheriff, 1984).

The data are summed along different slopes, each of which yields a separate trace of the transform. Equation 1 was the formula used to do slant stack.

$$u(p, \tau) = \int_{-\infty}^{\infty} u(x, \tau + px)\,dx. \qquad (1)$$

Figure 24 illustrates this procedure. The variable, τ, is the time at which a line of slope p intersects the time axis at zero offset. The magnitude at a particular τ is the summation of all data points which are tangent to that line. The length of the zone of tangency of the field-file data points with the line of slope, p, determines the magnitude at position τ (Claerbout, 1985).

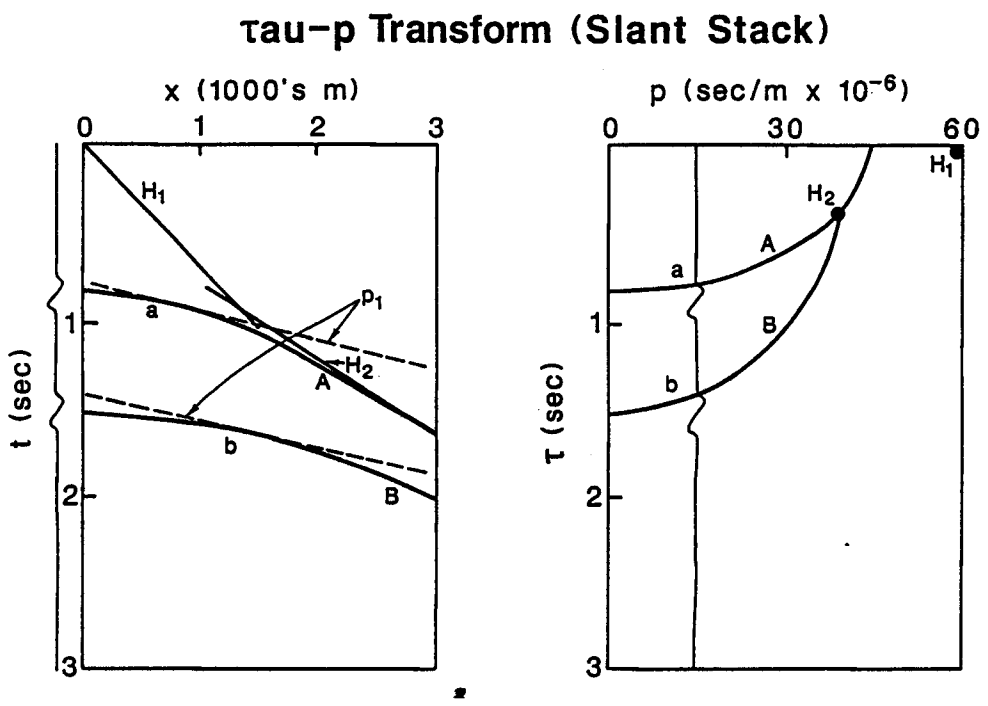

Figure 24. a). This simple field file contains two reflections, A and B, and two refractions, H1 and H2. When the transform is applied, data are summed along lines with slope, p, (dashed lines). The variable, tau, is the projection of these lines onto the zero-offset axis. The magnitude at a particular tau is the sum of the field-file traces along the straight lines. A trace representing the summation along lines of slope p1 is shown to the right of the figure. b). The trace shown in a) is at its proper position in this figure which is the tau-p domain representation of the field file. Reflections A and B are converted to ellipses, while refractions H1 and H2 are converted to points (from Tatham et al., 1982).

In tau-p space, events become separated. Reflections with hyperbolic moveout are converted to ellipses which do not cross each other while events with linear moveout such as ground roll transform to points or to small regions. In Figure 24, the reflections represented by letters A and B transform from hyperbolas in x-t space to ellipses A and B respectively in tau-p space. Refractions H1 and H2 transform to points in tau-p space. Slant stack acts as a velocity filter in that it allows one to keep or to eliminate events based on their velocity. The first step is to choose the minimum desired velocity and find its corresponding p-value. Since p is the inverse of the velocity, the minimum velocity value will be the maximum p-value. Only data between a specified minimum value of p and a maximum value of p are transformed into the tau-p domain. The rest of the data are rejected. Upon an inverse transformation back to the x-t domain, only the events with velocities (slopes) in the chosen range will be present. For this data, the p-values were chosen so that groundroll, air-coupled wave, and far-offset slope of reflections were eliminated. The algorithm used in the forward transform is also used in the inverse transform. The difference is that the data are stacked along slopes representing different offset values rather than different slownesses.

The result of applying slant stack was that reflections were enhanced when the data were transformed back into x-t space. In Figure 25, note the absence of the air-coupled wave and groundroll.

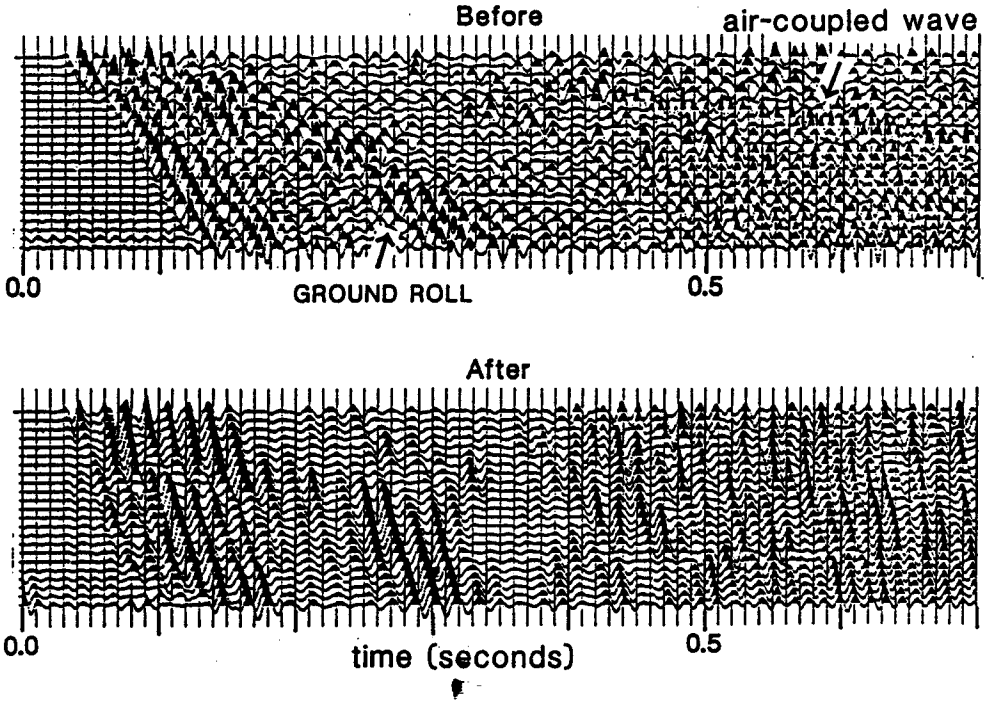

Figure 25. Application of slant stack velocity filter to the field file data eliminated the ground roll and the air-coupled wave, thus improving the data quality.

APPENDIX F

COMPLEX TRACE ANALYSIS

The following discussion is condensed from these references: (Bracewell, 1965, Taner and Sheriff, 1977, Taner et al., 1979, Sheriff and Geldart, 1983, Sheriff, 1980).

Complex trace analysis is one of many techniques used to aid seismic data interpretation. In signal analysis, data are commonly transformed from one domain to another. One such transformation is the Fourier transform in which the data are transformed from the time domain to the frequency domain and back again without any loss of information. The Fourier transform will display average properties of a large portion of a trace. Amplitude and phase spectra may be determined from sine waves which are fitted to the trace with correlation techniques. Thus, these spectra may be displayed over the entire frequency domain of the trace. If more local variation is desired, then complex trace analysis can be applied to the data. That is, certain quantities, called complex trace attributes, of the data may be calculated at each sample point rather than as averages over the entire trace. Attributes commonly used are instantaneous amplitude (reflection strength), instantaneous phase, instantaneous frequency, weighted average frequency, and polarity. Of

these, instantaneous amplitude, instantaneous phase, and instantaneous frequency attributes were applied to the data.

In complex trace analysis, the conventional seismic trace, x(t), is thought of as the real part of a complex, or analytic, trace, f(t).

$$f(t) = x(t) * iy(t). \qquad (2)$$

The imaginary part, y(t), which is called the quadrature component, has the same amplitude spectrum as the real part but differs in phase by 90 degrees. However, it is not calculated by simply multiplying the Fourier transform of the real seismic trace by the complex numbers '+i' or '-i'. This multiplication does change the phase by 90 degrees, but the transform back into the time domain will yield an imaginary trace. The quadrature trace is obtained by multiplying the transform of the real trace, $X(\omega)$, by a filter, $Q(\omega)$, which is equal to either '$i\,sgn(\omega)$' or '$-i\,sgn(\omega)$' where '$sgn(\omega)$' is equal to '1' for positive values of ω and '-1' for negative values of ω. A real trace will be obtained upon the transformation back to the time domain. Since multiplication in the frequency domain is equivalent to convolution in the time domain, the

quadrature trace can also be obtained by convolving the real trace with the quantity $(1/\pi t)$ as shown by Equation 3.

$$\begin{aligned} y(t) &= \text{IFT}[Y(\omega)]. \\ &= \text{IFT}[X(\omega)Q(\omega)]. \\ &= \text{IFT}[-iX(\omega)\,\text{sgn}(\omega)]. \\ &= x(t) * 1/\pi t. \end{aligned} \qquad (3)$$

where FFT = fast Fourier transform.

IFT = inverse Fourier transform.

Another way to calculate the quadrature trace is to do a Hilbert transform of the real trace as shown by Equation 4.

$$y(t) = (1/\pi)\,\text{P.V.}\int_{-\infty}^{\infty} \frac{f(t)}{\tau - t}\,dt.$$

where (4)

$$\text{P.V.}\int_{-\infty}^{\infty} = \lim\left[\int_{-\infty}^{\tau-\varepsilon} + \int_{\tau+\varepsilon}^{\infty}\right].$$

Figure 26 graphically shows the relationship which exists among the analytic, real, and quadrature traces. The analytic trace is a rotating vector which can be projected onto an imaginary plane to give the quadrature trace and onto a real plane to give the real or actual seismic trace. The analytic trace, f(t), can be calculated

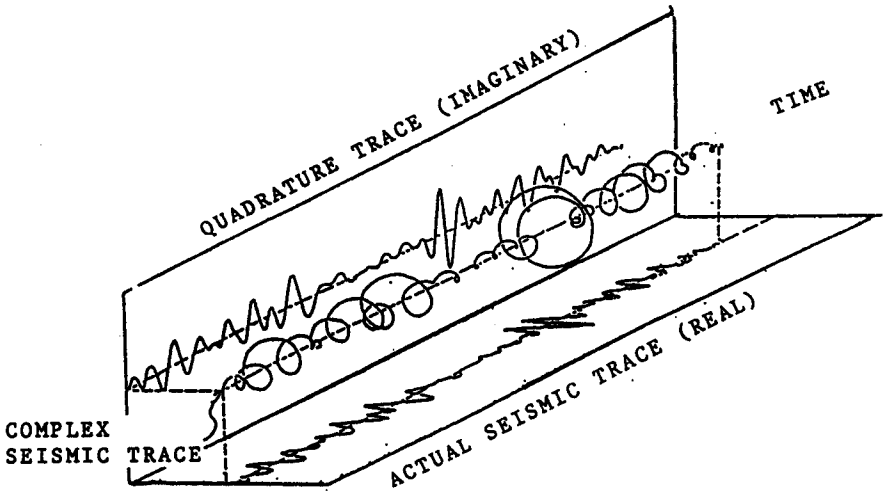

Figure 26. Relationship among the analytic, or complex, trace, the quadrature trace, and the actual seismic trace is shown. The actual and quadrature traces are the projection of the complex trace, a rotating vector, onto the real and imaginary planes respectively (from Taner and Sheriff, 1977).

from the seismic trace as described here. The first step is to take the Fourier transform of the seismic trace (Equation 5a). Then, the transform is multiplied by the filter, $Q(\omega)$, to obtain the quadrature trace (Equation 5b). Finally, the transform of the real trace becomes the real part of the analytic trace while the transform of the quadrature trace becomes the imaginary part of the analytic trace (Equation 5c).

$$X(\omega) = FFT[x(t)]. \tag{5a}$$

$$Y(\omega) = X(\omega)Q(\omega). \tag{5b}$$

$$\begin{aligned} f(t) = IFT[F(\omega)] &= IFT[X(\omega) + iY(\omega)]. \\ &= IFT[X(\omega) + iQ(\omega)X(\omega)]. \\ &= IFT[X(\omega)[1 + iQ(\omega)]]. \end{aligned} \tag{5c}$$

Since $Q(\omega)$ is chosen to be equal to the quantity, '$isgn(\omega)$' or '$-isgn(\omega)$', then $F(\omega)$ will be equal to zero for negative frequencies and will have double the amplitude spectrum of the real trace for positive frequencies.

$$\begin{aligned} \text{Let } Q(\omega) &= -isgn(\omega). \\ F(\omega) &= X(\omega)[1 + sgn(\omega)]. \\ &= 0. \qquad \omega < 0 \\ &= 2X(\omega). \quad \omega > 0 \end{aligned} \tag{6}$$

An inverse transform back to the time domain yields the analytic trace, f(t). In summary, the analytic trace, f(t), can be obtained by taking the Fourier transform of the real trace, doubling the amplitudes for positive frequencies, zeroing the amplitudes for negative frequencies, and then doing an inverse Fourier transform back to the time domain.

The analytic trace can be expressed by the following equation.

$$f(t) = A(t)\ e^{i\theta(t)}. \qquad (7)$$

The amplitude of the envelope, or the instantaneous amplitude, is given by A(t), while the instantaneous phase is expressed by $\theta(t)$. The instantaneous amplitude and the instantaneous phase attributes are determined from the real and quadrature traces.

$$A(t) = [x^2(t) + y^2(t)]^{1/2} = |f(t)|. \qquad (8a)$$

$$\theta(t) = \tan^{-1} [y(t)/x(t)]. \qquad (8b)$$

As shown by these equations, the values A(t) and $\theta(t)$ are not averages calculated over many samples. Instead, they are calculated at each sample point. The derivative of the instantaneous phase with respect to time is defined as the

instantaneous frequency. In simpler terms, the instantaneous frequency is the time rate of change of the instantaneous phase.

APPENDIX G

MIGRATION

A combination of ideas from the following works were used in this section: (Chun and Jacewitz, 1981, Sheriff and Geldart, 1983, Yilmaz, 1987).

Reflections on an unmigrated, stacked seismic section appear to be located spatially beneath the shotpoint as if the energy travelled vertically from shot to reflector and back to receiver. In reality, unless the reflector is horizontal, this is not the case. If reflectors have a dip of greater than about five degrees, then distortion of the true geology will occur. The extreme example of this is that a vertical reflector will appear to dip 45 degrees on a seismic section. In Figure 27, a reflection from point A' on the dipping bed will appear to be located at position A on a depth section. Migration is a technique which repositions reflectors at their true spatial locations. Therefore, point A will be moved to point A' after migration. As a result of migration, reflectors move updip and increase in dip. Thus, the curvature of anticlines will increase, while the curvature of synclines will decrease after migration has been applied.

The most common migration techniques are diffraction stack, finite difference, and frequency-domain migration. No method works perfectly for all cases. Frequency-domain

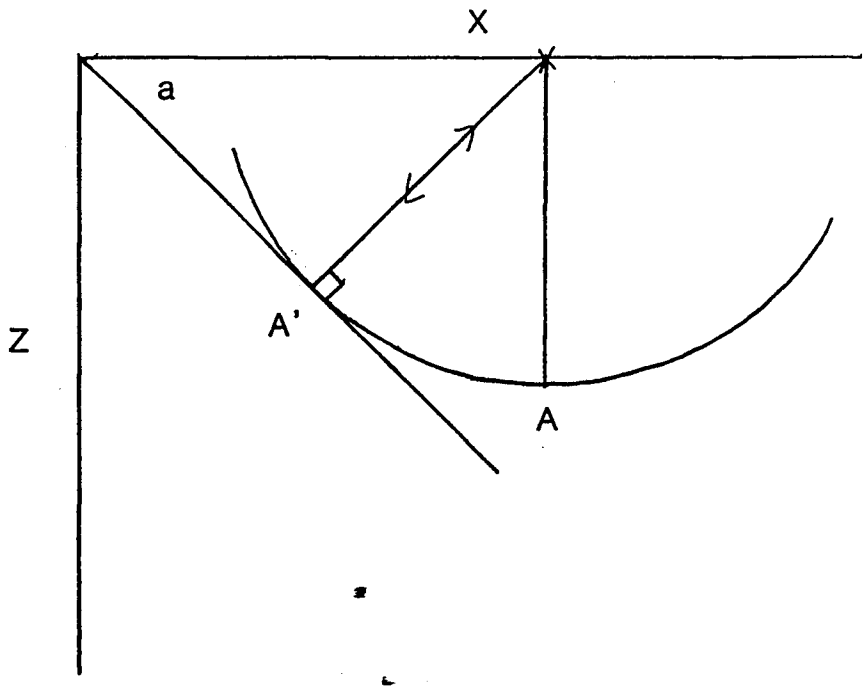

Figure 27. On an unmigrated seismic depth section, a reflection from the bed at point 'A'' will appear at point 'A', which is directly beneath the shotpoint. Migration will move the reflection from point 'A' to its true spatial location at point 'A''.

migration, also called F-K migration, was the technique used for this data set and works well in cases of low signal-to-noise ratios, steep dip, and reasonably constant velocity. Computing time is much less than with other methods. One disadvantage is that cases of widely-varying velocity are not handled very well. A seismic reflection will be moved horizontally a distance which is proportional to the migration velocity squared. The migration velocity also affects the angle of dip after migration. If the migration velocity is incorrect, then the reflection will be moved to the wrong place (Chun and Jacewitz, 1981). The earth is not a constant velocity medium. However, if the velocity doesn't vary too drastically, and if the unmigrated dip of the reflectors is close to zero, then the constant velocity algorithm can be applied with acceptable results. The Stolt constant velocity algorithm was used for my data set even though velocities varied both vertically and horizontally. The migration velocity was chosen to be 13 000 ft/sec.

The first step in this type of migration is a two-dimensional Fourier transform into the K_x-ω plane. This process transforms dipping reflectors in the x-t plane to lines in the K_x-ω plane which are perpendicular to the dip of the reflector. All events having the same dip are mapped to the same line in the K_x-ω plane and are migrated

together which makes computations easier and quicker in the frequency domain than in the x-t plane where events are usually scattered. Migration converts events in the K_x-ω plane to the K_x-K_z plane where K_z is the vertical wavenumber associated with depth. Figure 28 shows how this migration technique works. The premigrated event has been superimposed from the K_x-ω plane onto the K_x-K_z plane for easier viewing. Line V_b is the transform of the unmigrated dipping reflector, and it makes an angle, b, with the ω-axis. A straight line can be drawn from point A on the K_z axis to intersect the line V_b at point B. At this stage, point B is projected vertically downward to point C on a circle which has a radius of OA. A line drawn from the origin, O, through point C, represents the migrated reflector in the K_x-K_z domain. The dip angle after migration is angle 'a' which is steeper than the unmigrated dip angle, as expected. Geometrically, the above procedure satisfies the relationship (shown by Equation 9) existing between the migrated and unmigrated dip angles and preserves the dip in both cases.

$$\sin a = \tan b. \qquad (9)$$

An inverse transform back to the x-z domain yields the migrated reflector. Spatial frequency, or frequency in the

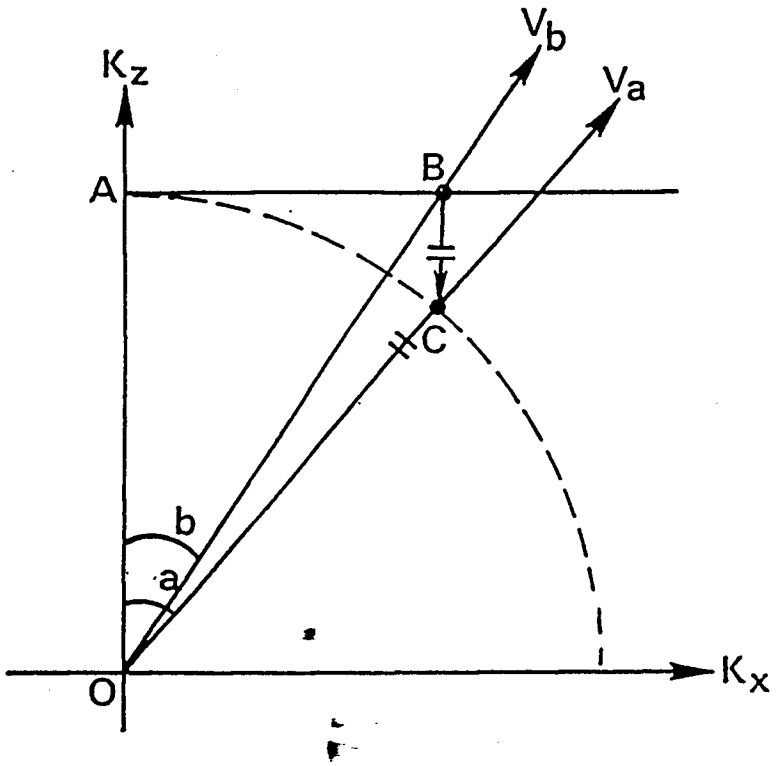

Figure 28. Procedure for frequency-wavenumber migration. Line V_b is an unmigrated reflector with dip 'b', while line V_a is the migrated reflector with steeper dip 'a'.

x-direction, is preserved in migration because each line, or reflector, is rotated about its intersection with the surface. The vertical projection downward from B to C in Figure 28 results in a lowering of frequency along the time axis.